International Forum on Aeroelasticity and Structural Dynamics
IFASD 2019
9-13 June 2019, Savannah, Georgia, USA

# A MULTI-OBJECTIVE OPTIMIZATION FRAMEWORK FOR HYPERSONIC AEROTHERMOELASTIC SCALING LAWS AND ITS APPLICATION TO SKIN PANELS

**Daning Huang**[1] **and Peretz P. Friedmann**[1]

[1]Department of Aerospace Engineering
The University of Michigan, Ann Arbor, MI, 48109

**Keywords:** hypersonic aerothermoelasticity, numerical scaling laws, multi-objective Bayesian optimization

**Abstract:** This study describes the development of an optimization framework for generating hypersonic aerothermoelastic scaling laws using a novel two-pronged approach. The approach combines classical scaling based on dimensional analysis with augmentation from numerical simulations of the specific problem. Combined comparison and adjustment of the full-scale prototype and the scaled model yields the refinement of the scaling laws. The search for an aerothermoelastically scaled model is formulated as an multi-objective optimization problem, which is solved using a multi-objective Bayesian optimization algorithm. The effectiveness of the two-pronged approach is demonstrated by its application to the development of refined hypersonic aerothermoelastic scaling laws for a composite skin panel configuration.

## List of Symbols

*Latin Symbols*

| | |
|---|---|
| $\mathbf{A}, A_{xx}$ | Extensional stiffness matrix for composite shell and its first element |
| $\mathbf{B}, B_{xx}$ | Extension-bending stiffness matrix for composite shell and its first element |
| $Bi$ | Biot number |
| $\bar{B}$ | Nose bluntness similarity parameter |
| $C$ | Acquisition function |
| $\mathbf{c}_E, \mathbf{c}_I$ | Equality and inequality constraints |
| $c_p$ | Specific heat capacities at constant pressure |
| $c_u, c_T$ | Weights for structural and thermal objectives |
| $\mathbf{D}, D_{xx}$ | Bending stiffness matrix for composite shell and its first element |
| $\mathcal{D}$ | Data set |
| $\mathbf{d}$ | Design variables |
| $d$ | Radius of the blunt nose of a slender body |
| $\mathbb{E}$ | Statistical expectation |
| $E$ | Young's modulus |
| $\mathcal{F}$ | Pareto front |
| $\overline{\mathcal{F}}$ | Pareto set, i.e. a set of Pareto optimal solutions |
| $Fo$ | Fourier number |

| | |
|---|---|
| $\mathcal{H}$ | Hypervolume of Pareto front |
| $H$ | Altitude |
| $\mathbf{h}, h_i$ | Thicknesses of lamina of a composite shell, and the $i$th laminae |
| $h$ | Shell thickness |
| $\mathcal{I}$ | Improvement function |
| $I_1, I_2, I_3$ | Moments of inertia of the composite shell |
| $I_{\mathcal{H}}$ | Hypervolume indicator of Pareto front |
| $\mathbf{J}$ | Vector of objectives |
| $J_u, J_T, J_s$ | Errors in the nondimensional aerothermoelastic response |
| $\mathbf{k}, k$ | Thermal conductivity |
| $L$ | Characteristic length |
| $L_{le}$ | Length of rigid wall upstream of the panel |
| $\mathbf{M}_T, M_{Tx}$ | Thermal internal in-plane moments and the first element |
| $M$ | Mach number |
| $\mathbf{N}_T, N_{Tx}$ | Thermal internal in-plane forces and the first element |
| $\mathcal{N}$ | Gaussian distribution |
| $N_t$ | Number of time steps |
| $\mathbf{n}$ | Normal vector |
| $P$ | Probability |
| *Pr* | Prandtl number |
| $p$ | Pressure |
| $\mathbf{Q}$ | Stiffness matrix in lamina constitutive relation |
| $\dot{q}$ | Heat flux |
| $R_i$ | Curvature in $i$ direction |
| *Re* | Reynolds number |
| $\mathbf{S}, S_{xx}$ | Transverse shear stiffness matrix for composite shell and its first element |
| $\mathcal{S}, \mathcal{S}_g$ | Function for combining multiple objectives |
| $\mathbf{T}, T$ | Temperature |
| $T_w$ | Wall temperature |
| $T_{ini}$ | Initial temperature |
| $T_{rad}$ | Radiation temperature |
| $T_{cr}$ | Temperature associated with the first buckling mode |
| $\Delta T$ | Temperature increase |
| $t$ | Time |
| $\Delta t$ | Time step size |
| $\mathbf{u}, u$ | Structural displacements |
| $\mathbf{u}_w$ | Thickness distribution of a slender body |
| $\mathbf{V}, V$ | Flow velocity |
| $\mathbf{x} = [x, y, z]$ | Cartesian coordinates |

*Greek Symbols*

| | |
|---|---|
| $\boldsymbol{\alpha}, \alpha$ | Thermal expansion coefficients |
| $\gamma$ | Heat capacity ratio |
| $\varepsilon$ | Surface emissivity |
| $\theta$ | Inclination angle |
| $\bar{\lambda}_F$ | Nondimensional dynamic pressure |

| | |
|---|---|
| $\boldsymbol{\mu}$ | Mean of Gaussian distribution |
| $\mu$ | Viscosity |
| $\nu$ | Poisson's ratio |
| $\bar{\Xi}$ | Boundary layer similarity parameter |
| $\xi$ | Geometric scale |
| $\rho$ | Density |
| $\boldsymbol{\Sigma}, \boldsymbol{\sigma}$ | Covariance matrix of Gaussian distribution, and the vector of standard deviations |
| $\sigma$ | Standard deviation in Gaussian distribution |
| $\upsilon$ | Coefficient for exploitation-exploration balance |
| $\Phi$ | Cummulative density functions |
| $\boldsymbol{\Psi}_u, \boldsymbol{\Psi}_T$ | Projection matrices whose columns are structural and thermal modes, respectively |

*Subscripts and superscripts*

| | |
|---|---|
| $\square_{bc}$ | Quantities related to boundary conditions |
| $\square_{ext}$ | Quantities related to external loading |
| $\square_F$ | Quantities related to the fluid solution |
| $\square_{ref}$ | Quantities for reference |
| $\square_S$ | Quantities related to the structural solution |
| $\square_T$ | Quantities related to the thermal solution |
| $\square_\infty$ | Quantities related to freestream |
| $\square_0$ | Quantities related to stagnation state |
| $\square^f$ | Properties of the fluid |
| $\square^m$ | Quantities related to the scaled model |
| $\square^p$ | Quantities related to the prototype |
| $\square^s$ | Properties of the solid |
| $\square^{sur}$ | Quantities related to surrogate |
| $\widehat{\square}$ | Reference quantity for non-dimensionalization |
| $\overline{\square}$ | Nondimensional quantity |
| $\|\|\mathbf{f}\|\| = \left(\sum_i f_i^2\right)^{1/2}$ | The $l^2$ norm |

*Acronyms*

| | |
|---|---|
| ADflow | Automatic Differentiation flow solver |
| ASL | Aerothermoelastic Scaling Laws |
| BHCJ | Boeing Hypersonic Commercial Jet |
| BO | Bayesian Optimization |
| CFD | Computational Fluid Dynamics |
| EI | Expected Improvement |
| HTF | Hypersonic Tunnel Facility |
| HV | HyperVolume |
| HYPATE | HYPersonic AeroThermoElasticity simulation environment |
| LCB | Lower Confidence Bound |
| LSA | Linearized Stability Analysis |
| MO | Multi-objective Optimization |

| | |
|---|---|
| MOBO | Multi-Objective Bayesian Optimization |
| NS | Navier-Stokes |
| OLH | Optimial Latin Hypercube |
| POD | Proper Orthogonal Decomposition |
| PoI | Probability of Improvement |
| ROM | Reduced Order Model |
| SO | Single-objective Optimization |
| SBO | Surrogate-Based Optimization |
| WM | Weighted Metric |

## 1 INTRODUCTION, BACKGROUND AND OBJECTIVES

Airbreathing hypersonic vehicles have the potential to revolutionize global transportation by vastly reducing the traveling time between distant locations. The past decade has witnessed strong, revived interest in reusable airbreathing hypersonic launch vehicles for low-cost space exploration as well as rapid response to global military threats [1–4]. Airbreathing hypersonic vehicles are exposed to extreme aerothermodynamic environments that involve high aerodynamic loading and heating, leading to degradation of material properties. The thermal stress introduced by the temperature gradients and geometrical constraints can affect structural integrity and cause structural instabilities, such as buckling, panel flutter, and control surface flutter. Therefore, the determination of aerothermoelastic characteristics is critical for the design of hypersonic vehicles.

One approach for determining the aerothermoelastic characteristics is aerothermoelastic testing. Aerothermoelastic testing refers to the construction of a scaled version of the prototype vehicle and its direct insertion into a high-stagnation-temperature wind tunnel where the aerothermoelastic model can be exposed to aerodynamic heating and loading simultaneously. Once such wind tunnel tests were available, the test data obtained on scaled models could be extrapolated to full-size vehicles, resulting in a dramatic reduction in the cost of hypersonic aerothermoelastic flight testing, as well as a shortened design cycle of hypersonic vehicles.

Work conducted on hypersonic vehicles in early 1960's has resulted in landmark papers [5–7] on scaling laws that can be used for constructing aerothermoelastically scaled models and mapping of the experimental results back to the full-scale prototype. The aerothermoelastic scaling laws (ASL) enable wind tunnel tests up to $M_\infty \leq 3.5$ and $T_0 \leq 1000°F \approx 811K$. However, modern hypersonic vehicles are expected to operate at much higher Mach numbers and in wider range of temperatures, as illustrated in Fig. 1. Experimental vehicles such as the X-43 [8] and the X-51 [9] have flown over Mach 4.5-6 at altitudes from 15 km to 33.5 km. The SR-72 is expected to cruise at Mach 6 at an altitude of 24.3 km [10]. The Boeing Hypersonic Commercial Jet (BHCJ) is expected to cruise at Mach 5 at an altitude of 27 km [11]. As a result, the range of aerothermoelastic testing has to be extended from the high supersonic flow regime to the hypersonic flow regime $M_\infty \leq 10$ and $T_0 \leq 3000K$. However, Ref. [7] has concluded that complete hypersonic aerothermoelastic similarity is impossible to achieve for scale ratios that differ from unity.

Lack of hypersonic ASL has resulted in the use of "restricted purpose" testing approaches and "incomplete" aerothermoelastic testing [6, 7]. Restricted purpose testing implies a study of the aerothermoelastic problem assuming that the coupling between the aerodynamic pressure, aerodynamic heating, heat conduction and stress-deflection phenomena is weak. However, the fluid-thermal-structural interactions cannot be decoupled in modern hypersonic vehicles since they are based on an integrated airframe-propulsion concept, which enhances the interactions between the various components [12]. Incomplete aerothermoelastic testing refers to the use of additional means, other than aerodynamics, to provide loading or heating. This requires *a priori* knowledge of the loading and heating on the full-scale vehicle, as well as the ability to accurately apply these loads at the appropriate locations as a function of time, which is difficult to achieve in practice. The barriers associated with hypersonic aerothermoelastic testing have been one of the factors contributing to problems encountered during the development of air-breathing hypersonic vehicles in the past, such as failures in flight as well as high temperature structural testing.

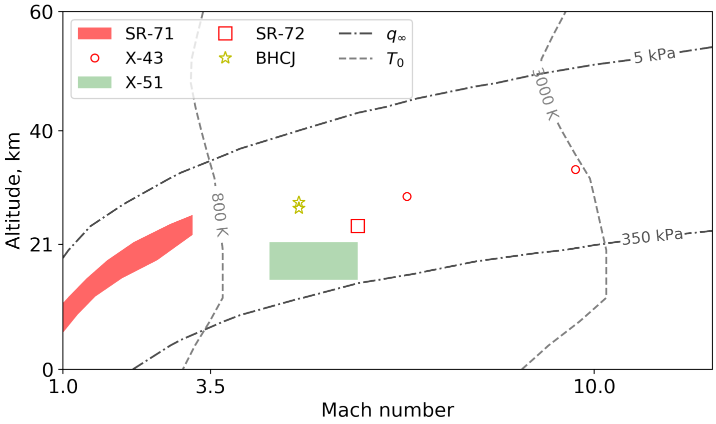

Figure 1: Flight envelopes of typical supersonic and hypersonic vehicles.

In addition to the lack of ASL, another issue associated with hypersonic aerothermoelastic testing is the scarcity of appropriate wind tunnel facilities for the tests beyond the high supersonic flow regime. An ideal wind tunnel has to meet three basic requirements: (1) high stagnation pressure ($p_0 \geq 0.5\text{MPa}$), (2) high stagnation temperature ($T_0 \geq 800K$), and (3) sufficiently long operating time period (at least on the order of minutes). The first two requirements ensure the simultaneous reproduction of the hypersonic aerodynamic loading and heating conditions and the third requirement ensures sufficient time for the development of the thermal responses in the scaled model that is critical to aerothermoelastic testing. Figure 2 illustrates the typical operational time period and stagnation temperature of different types wind tunnels [13, 14]. Only some of the blow-down and continuous wind tunnels can potentially satisfy the basic requirements of hypersonic aerothermoelastic testing. Furthermore, two additional requirements are desirable: (1) the test section should be sufficiently large to accomodate the scaled model; (2) the working fluid should be inert gas, e.g. dry air or Nitrogen-Oxygen mixture, to avoid reactive products [14]. When accounting for these requirements, there are only a limited number of wind tunnels that can be potentially used for hypersonic aerothermoelastic testing [14–17], as illustrated in Fig. 3.

Recently, there is renewed interest in developing models for aerothermoelastic testing in high supersonic and hypersonic wind tunnels [14, 18]. In these studies, scaled skin panel models are designed with the aid of numerical simulation tools so as to obtain the desired aerothermoelastic response in the wind tunnel. However, the primary goal of these studies is not to achieve aerothermoelastic scaling. Instead, the goal is to develop skin panel models that are quite flexible, such that the interaction between the high-speed flow and the panel deformation becomes observable in the wind tunnel. The response observed on such wind tunnel models is not representative of the realistic aerothermoelastic response of the skin panels on a hypersonic vehicle.

To summarize, success in the development of scaling laws for hypersonic aerothermoelasticity has not been achieved yet. Therefore hypersonic aerothermoelastic testing is non-existent. This situation limits substantially our understanding of the aerothermoelastic behavior of hypersonic structures.

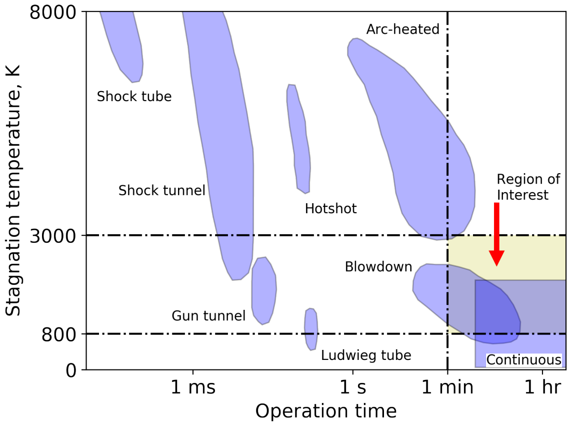

Figure 2: Capabilities of various types of wind tunnels.

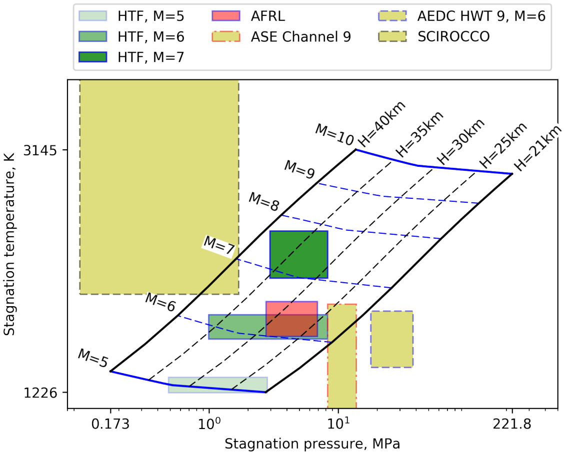

Figure 3: Envelope of testing conditions of several wind tunnels.

In the previous studies [19–21], a novel methodology was proposed in order to overcome the difficulties associated with the hypersonic aerothermoelastic testing by developing “numerical” ASL. The methodology is based on the two-pronged approach [22] that combines the classical approach with modern simulation based on computational aerothermoelasticity, as illustrated in Fig. 4. On the left-hand branch, basic scaling requirements are established using dimensional analysis, in a manner that resembles the classical procedure in Ref. [7]. On the right-hand branch, complete aerothermoelastic solutions for the prototype (i.e. full scale) as well as the scaled model are obtained using numerical aerothermoelastic simulation. From the comparison and adjustment of these two models, the “numerical similarity solutions” are generated to replace the analytical similarity solutions for refined scaling laws. The process of model adjustment is formulated as an optimization problem, where the design variables are selected to correspond to the most important parameters needed for the refined simulation that differ from those employed when generating the model based on classical similarity. Eventually, the numerical scaling laws for the specialized cases can be obtained without recourse to the *ad hoc* assumptions used in the classical approach, which overcomes the difficulties associated with hypersonic aerothermoelastic testing. In Refs. [19–21], the effectiveness of the two-pronged approach for deriving numerical ASL was demonstrated by the scaling of a skin panel in hypersonic flow. The similarity in the aerothermoelastic stability boundary between the prototype and the model was successfully obtained by adjusting a single variable consisting of the upstream plate length.

The current study is a sequel to our previous studies [19–21], aiming to generalize the optimization framework for the development of numerical scaling laws of aerothermoelastic responses. The specific objectives of the paper are:

1. To present a systematic dimensional analysis of the aerothermoelastic response of a modern composite hypersonic structure.
2. To develop a multi-objective optimization framework using the two-pronged approach that enables the generation of refined hypersonic ASL.
3. To apply the optimization framework to generate aerothermoelastically scaled models of a composite skin panel in hypersonic flow that are suitable for testing under realistic wind tunnel conditions.

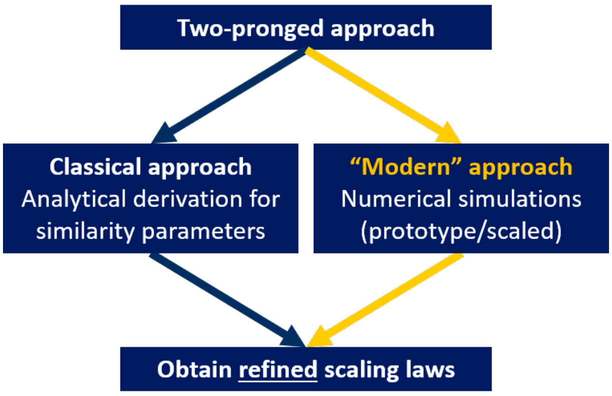

Figure 4: Schematic illustration of the two-pronged approach.

## 2 ANALYTICAL AEROTHERMOELASTIC SCALING LAWS REVISITED

In the literature, only partial successes were achieved in the development of hypersonic ASL [5–7]. The aerothermoelastic similarity parameters that need to be satisfied are derived from the dimensional analysis of the general equations for stress, displacement and temperature distribution of an isotropic slender body immersed in a hot, flowing gas. In this section, following the analytical approach in Refs. [5–7], the derivation of similarity parameters is extended for the aerothermoelastic response of a modern composite hypersonic structure. The major similarity parameters are identified as required for the left-hand branch of the two-pronged approach. Finally, the conflicts in analytical aerothermoelastic scaling are identified and possible solutions to these conflicts are proposed.

### 2.1 The Thermal Problem

The governing equation of heat transfer in an anisotropic solid body is [23],

$$\rho^s(\mathbf{x},T)c_p^s(\mathbf{x},T)\dot{T} - \nabla\cdot(\mathbf{k}^s(\mathbf{x},T)\cdot\nabla T) = 0 \tag{1}$$

and the boundary and initial conditions are as follows,

$$\text{On body surface :}\quad -\mathbf{n}\cdot\mathbf{k}^s(\mathbf{x},T)\cdot\nabla T = \dot{q}_{bc}(\mathbf{x},T,t) = \dot{q}_F(\mathbf{x},T,t) + \dot{q}_{ext}(\mathbf{x},T,t) \tag{2a}$$

$$\text{At } t = 0 :\quad T(\mathbf{x}) = T_{ini}(\mathbf{x}) \tag{2b}$$

where the density, thermal capacity and conductivity are inhomogenous and temperature dependent. The surface heat flux $\dot{q}_{bc}$ is due to aerodynamic heating $\dot{q}_F$ and other heat sources $\dot{q}_{ext}$, such as radiation.

The non-dimensionalization of Eqs. (1)-(2) results in the following similarity parameters,

$$Fo = \frac{\hat{k}^s \hat{t}}{\hat{\rho}^s \hat{c}_p^s \hat{L}_3^2}, \quad Bi = \frac{\hat{q}\hat{L}_3}{\hat{k}^s \hat{T}_T}, \quad \frac{\hat{L}_3}{\hat{L}_1}, \quad \frac{\hat{L}_3}{\hat{L}_2} \tag{3a}$$

$$\bar{\rho}^s \bar{c}_p^s, \quad \bar{\mathbf{k}}^s, \quad \bar{T}_{ini}, \quad \bar{q}_{bc} \tag{3b}$$

where the quantities with a hat $(\widehat{\square})$ are reference values and the quantities with a bar $(\overline{\square})$ are nondimensional.

In Eq. (3a), the first quantity is the Fourier number, a dimensionless time representing the ratio between the rate of heat conduction to the rate of energy stored by capacitance [24, 25]. It defines the time scale of the thermal problem. The second quantity is the Biot number that characterizes the heat transfer resistance of the body. The quantities $\frac{\hat{L}_3}{\hat{L}_1}$ and $\frac{\hat{L}_3}{\hat{L}_2}$ require the similarity in geometrical configuration. In Eq. (3b), the first two quantities require the similarity in the material properties as functions of temperature and spatial coordinates. Note that $\bar{\mathbf{k}}^s$ is a $3 \times 3$ symmetric matrix, and contains 6 independent similarity parameters. The last two quantities define the distribution of initial temperature field and the heat flux, respectively.

For heat transfer in a composite shell structure, one can choose $\hat{L}_1 = \hat{L}_2 = \hat{L}$ as the length scale of the shell and $\hat{L}_3 = \hat{h}$ as the thickness of the shell, simplifying the similarity parameters in Eq. (3),

$$Fo = \frac{\hat{k}^s \hat{t}}{\hat{\rho}^s \hat{c}_p^s \hat{h}^2}, \quad Bi = \frac{\hat{q}\hat{h}}{\hat{k}^s \hat{T}_T}, \quad \frac{\hat{h}}{\hat{L}} \tag{4a}$$

$$\bar{\rho}^s \bar{c}_p^s, \quad \bar{\mathbf{k}}^s, \quad \bar{T}_{ini}, \quad \bar{q}_{bc} \tag{4b}$$

For a composite shell, the reference values for $\rho^s c_p^s$ and $\mathbf{k}^s$ are defined as,

$$\hat{\rho}^s \hat{c}_p^s = \int_{\hat{h}} \rho^s(\mathbf{x}, \hat{T}_T) c_p^s(\mathbf{x}, \hat{T}_T) \mathrm{d}z \tag{5a}$$

$$\hat{k}^s = \left( \int_{\hat{h}} \frac{\mathrm{d}z}{k_{11}^s(\mathbf{x}, \hat{T}_T)} \right)^{-1} \hat{h} \tag{5b}$$

where $k_{11}^s$ is the first element of $\mathbf{k}^s$, and the reference thermal temperature $\hat{T}_T$ is determined by the dimensional analysis of the aerothermoelastic problem.

## 2.2 The Structural Problem

The governing equations for the shell structure representing the skin on the surface of a hypersonic vehicle are based on the composite shallow shell theory with first-order shear deformation theory and geometrical nonlinearity [26]. The panel is subjected to a transverse distributed loading $p = p_F + p_{ext}$, which consists of aerodynamic pressure and other sources of loading. In the non-dimensionalization, the loading $p$ is treated as a single variable.

The non-dimensionalization of the structural problem results in the following similarity parameters,

$$\frac{\hat{I}\hat{L}^4}{\widehat{D}_{xx}\hat{t}^2}, \quad \bar{R}_x, \quad \bar{R}_y \tag{6a}$$

$$\bar{I}_1, \quad \frac{\hat{h}\bar{I}_2}{\hat{L}}, \quad \frac{\hat{h}^2\bar{I}_3}{\hat{L}^2} \tag{6b}$$

$$\overline{\mathbf{A}}, \quad \overline{\mathbf{B}}, \quad \overline{\mathbf{D}}, \quad \overline{\mathbf{S}}, \quad \overline{\mathbf{N}}_T, \quad \overline{\mathbf{M}}_T \tag{6c}$$

$$\frac{\widehat{A}_{xx}\hat{L}^2}{\widehat{D}_{xx}}, \quad \frac{\widehat{B}_{xx}\hat{L}}{\widehat{D}_{xx}}, \quad \frac{\widehat{S}_{xx}\hat{L}^2}{\widehat{D}_{xx}}, \quad \frac{\widehat{N}_{Tx}\hat{L}^3}{\widehat{D}_{xx}\hat{u}}, \quad \frac{\widehat{M_{Tx}}\hat{L}^2}{\widehat{D}_{xx}\hat{u}} \tag{6d}$$

$$\frac{\hat{p}\hat{L}^4}{\widehat{D}_{xx}\hat{u}}, \quad \bar{p}, \quad \frac{\hat{u}}{\hat{L}} \tag{6e}$$

In Eq. (6a), the first quantity defines the time scale of the structural problem, and the next two quantities represent the similarity in the geometrical configuration. The quantities in Eqs. (6b) and (6c) require similarity in material properties as functions of temperature and spatial coordinates. Note that $\overline{\mathbf{A}}$, $\overline{\mathbf{B}}$ and $\overline{\mathbf{D}}$ are $3 \times 3$ symmetric matrices, $\overline{\mathbf{S}}$ is a $2 \times 2$ symmetric matrix, and $\overline{\mathbf{N}}_T$ and $\overline{\mathbf{M}}_T$ are $3 \times 1$ vectors. Therefore, $\overline{\mathbf{A}}$, $\overline{\mathbf{B}}$ and $\overline{\mathbf{D}}$ each contain 6 independent similarity parameters, while $\overline{\mathbf{S}}$, $\overline{\mathbf{N}}_T$ and $\overline{\mathbf{M}}_T$ each contain 3 independent similarity parameters. The quantities in Eq. (6d) requires the similarity in the ratios of various elastic properties. Finally, in Eq. (6e), the first two quantities require the similarity in the distribution and the magnitude of the external loading. The quantity $\frac{\hat{u}}{\hat{L}}$ requires the similarity in the magnitude of the nonlinear deformation. The reference structural temperature $\hat{T}_S$, which is contained in the definitions of $\widehat{A}_{xx}$, $\widehat{B}_{xx}$, $\widehat{D}_{xx}$, $\widehat{S}_{xx}$, $\widehat{N}_{Tx}$, $\widehat{M_{Tx}}$ and $\hat{I}$, is determined from the consideration of the aerothermoelastic problem.

In the case of thin, isotropic, and homogeneous plate, the 41 similarity parameters in Eq. (6) reduce to 13 parameters,

$$\frac{\hat{I}\hat{L}^4}{\widehat{D}_{xx}\hat{t}^2} \tag{7a}$$

$$\bar{I}_1 \tag{7b}$$

$$\overline{A}_{xx}, \quad \overline{D}_{xx}, \quad \overline{N}_{Tx}, \quad \overline{M}_{Tx}, \quad \nu \tag{7c}$$

$$\frac{\widehat{A}_{xx}\hat{L}^2}{\widehat{D}_{xx}}, \quad \frac{\widehat{N}_{Tx}\hat{L}^3}{\widehat{D}_{xx}\hat{u}}, \quad \frac{\widehat{M_{Tx}}\hat{L}^2}{\widehat{D}_{xx}\hat{u}} \tag{7d}$$

$$\frac{\hat{p}\hat{L}^4}{\widehat{D}_{xx}\hat{u}}, \quad \bar{p}, \quad \frac{\hat{u}}{\hat{L}} \tag{7e}$$

The set of similarity parameters in Eq. (7) is equivalent to the classical results in Ref. [7] if the reference value for the elastic portion of the in-plane force is defined as,

$$\widehat{N} = \widehat{A}_{xx}\frac{\hat{u}}{\hat{L}} \tag{8}$$

### 2.3 The Fluid Problem

The fluid domain is governed by the complete unsteady Navier-Stokes (NS) equations for a compressible, viscous, heat-conducting, perfect gas [6, 7]. For hypersonic flow, the following nondimensional quantities are introduced to non-dimensionalize the NS equations.

$$\bar{x}_i = \frac{x_i}{\hat{L}}, \quad \bar{t} = \frac{t}{\hat{t}}, \quad \bar{T} = \frac{T}{\hat{T}_F}, \quad \bar{\mathbf{V}} = \frac{\mathbf{V}}{\hat{V}}, \quad \bar{\rho}^f = \frac{\rho^f}{\hat{\rho}^f}, \quad \bar{p} = \frac{p}{\hat{p}} \tag{9a}$$

$$\bar{\mu} = \frac{\mu}{\hat{\mu}}, \quad \bar{c}_p^f = \frac{c_p^f}{\hat{c}_p^f}, \quad \bar{k}^f = \frac{k^f}{\hat{k}^f} \tag{9b}$$

As suggested in Ref. [6], in hypersonic flow, it is more convenient to non-dimensionalize the NS equations using the stagnation conditions, instead of the free-stream conditions, because the following high-$M_\infty$ approximations are available at the stagnation point,

$$T_0 \approx \frac{V_\infty^2}{2c_{p0}^f f_T}, \quad f_T = \int_0^1 \bar{c}_p^f \mathrm{d}\left(\frac{T}{T_0}\right) \tag{10a}$$

$$p_0 \approx \frac{\gamma+3}{2(\gamma+1)} \rho_\infty V_\infty^2 \tag{10b}$$

The following quantities are chosen as the reference values,

$$\hat{V} = V_\infty, \quad \hat{\rho}^f = \rho_\infty, \quad \hat{p} = p_0 \tag{11a}$$

$$\hat{\mu} = \mu_0, \quad \hat{c}_p^f = c_{p0}^f, \quad \hat{k}^f = k_0^f \tag{11b}$$

The similarity parameters for the NS equations are [6],

$$\frac{V_\infty \hat{t}}{\hat{L}}, \frac{\hat{T}_F}{T_0} \tag{12a}$$

$$\mathit{Re}_0 = \frac{\rho_\infty V_\infty \hat{L}}{\hat{\mu}}, \mathit{Pr}_0 = \frac{\hat{c}_p^f \hat{\mu}}{\hat{k}^f}, \gamma \tag{12b}$$

$$\bar{\mu}, \bar{c}_p^f, \bar{k}^f \tag{12c}$$

$$\bar{\mathbf{u}}_w = \frac{\mathbf{u}_w}{\hat{u}} \tag{12d}$$

In Eq. (12a), the first quantity defines the time scale of the fluid problem, and the second quantity defines the reference temperature. The quantities in Eq. (12b) require similarity in the flow properties. Note that the freestream Mach number $M_\infty$ does not appear and this is a result of the Mach number independence principle in the hypersonic flow (pp. 107–111 of Ref. [27]). Equation (12c) requires the similarity in the gas properties as functions of temperature. Finally, the geometric similarity between the model and prototype is required.

The similarity parameters in Eq. (12) are rewritten for a slender body [28, 29], where concept of boundary layer can be used. The slender body is characterized by a small thickness ratio $\frac{\hat{u}}{\hat{L}} \ll 1$, which is typical of a skin panel. Note that the thickness distribution $\mathbf{u}_w$ accounts for both the geometry and the deformation. With a few simplifying assumptions for hypersonic flow and boundary layer, the similarity parameters for the surface pressure and the heat flux on a slender body are [6],

$$\frac{\hat{V}\hat{t}}{\hat{L}}, \quad \frac{\hat{T}_F}{T_0}, \quad \bar{T}_w = \frac{T_w}{\hat{T}_F}, \quad \bar{\mathbf{u}}_w \tag{13a}$$

$$\frac{\hat{p}\hat{L}}{\gamma p_\infty M_\infty \hat{u}}, \quad Re_0 Pr_0 \frac{\hat{k}^f \hat{V}^2}{\hat{q}\hat{c}_p^f \hat{L}} \tag{13b}$$

$$\bar{\Xi} = \frac{\hat{L}^2}{\hat{u}^2\sqrt{Re_0}}, \quad \bar{B} = k_B M_\infty^3 \frac{\hat{d}}{\hat{L}} \tag{13c}$$

$$Pr_0, \quad \gamma \tag{13d}$$

Four new similarity parameters are introduced in Eqs. (13a)-(13d). The two quantities in Eq. (13b) define the reference magnitudes of the pressure and the heat flux, respectively. In Eq. (13c), $\bar{\Xi}$ requires similarity in the boundary layer thickness. The parameter $\bar{\Xi}$ is important when the viscous interaction is strong, i.e. when the pressure distribution is significantly modified by the boundary layer. The parameter $\bar{B}$ is introduced to characterize the nose bluntness of the slender body, i.e. the sharpness of the leading edge, because the pressure distribution on the slender body is sensitive to the geometry of the nose, or the cross-section of the leading edge [7, 29]. In the parameter $\bar{B}$, $\hat{d}$ is the characteristic radius of the nose, and $k_B$ is a constant that depends on the nose geometry.

Finally, note that a few simplifying assumptions, such as laminar flow and perfect gas law, have been used when deriving the similarity parameters in Eq. (13) [6, 7]. Therefore, when more complex effects are present in the fluid problem, e.g. turbulent boundary layer and real gas effect, the similarity parameters in Eqs. (12) and (13) may not represent the correct scaling requirements for constructing a scaled model that satisfies hypersonic aerothermodynamic similarity.

### 2.4 The Aerothermoelastic Problem

The aerothermoelastic response of a hypersonic skin panel consists of the aeroelastic and aerothermal responses. The aeroelastic response is represented by the structural deformation and aerodynamic pressure distribution, while the aerothermal response is represented by the structural temperature and the aerodynamic heat flux distribution. This study focuses on the behavior of a typical structural component in hypersonic flow. Therefore, in the rest of this paper, the similarity in aerothermoelastic response refers to the similarity in the time history of the structural deformation and temperature.

From Eqs. (4), (6) and (13), the similarity parameters for the aerothermoelastic response of a skin panel are,

$$\text{Geometry}: \frac{\hat{h}}{\hat{L}}, \quad \bar{h}, \quad \frac{\hat{d}}{\hat{L}} \tag{14a}$$

$$\text{Time}: \mathit{Fo}, \quad \frac{\hat{I}\hat{L}^4}{\widehat{D}_{xx}\hat{t}^2}, \quad \frac{\hat{V}\hat{t}}{\hat{L}} \tag{14b}$$

$$\text{Coupling}: \begin{cases} \bar{\lambda}_F, \ \mathit{Bi}_F, \ \dfrac{\hat{u}_w}{\hat{L}}, \ \dfrac{T_w}{\hat{T}_S}, \ \dfrac{\hat{T}_T}{\hat{T}_S}, \ \dfrac{T_0}{\hat{T}_S}, \ \dfrac{\hat{T}_F}{\hat{T}_S} \\ \bar{p}_F, \ \bar{\dot{q}}_F, \ \bar{\mathbf{u}}_w, \ \bar{T}_w, \ \bar{T} \end{cases} \tag{14c}$$

$$\text{Thermal}: \begin{cases} \mathit{Bi}_{ext} = \dfrac{\hat{\dot{q}}_{ext}\hat{h}}{\hat{k}^s\hat{T}_T}, \ \bar{\dot{q}}_{ext} \\ \bar{\rho}^s\bar{c}_p^s, \ \bar{\mathbf{k}}^s \end{cases} \tag{14d}$$

$$\text{Structural}: \begin{cases} \dfrac{\widehat{A}_{xx}\hat{L}^2}{\widehat{D}_{xx}}, \ \dfrac{\widehat{B}_{xx}\hat{L}}{\widehat{D}_{xx}}, \ \dfrac{\widehat{S}_{xx}\hat{L}^2}{\widehat{D}_{xx}}, \ \dfrac{\widehat{N}_{Tx}\hat{L}^2}{\widehat{D}_{xx}}, \ \dfrac{\widehat{M_{Tx}}\hat{L}}{\widehat{D}_{xx}}, \ \bar{\lambda}_{ext} = \dfrac{\hat{p}_{ext}\hat{L}^3}{\widehat{D}_{xx}}, \ \bar{p}_{ext} \\ \bar{\mathbf{A}}, \ \bar{\mathbf{B}}, \ \bar{\mathbf{D}}, \ \bar{\mathbf{S}}, \ \bar{\mathbf{N}}_T, \ \bar{\mathbf{M}}_T, \ \bar{I}_1, \ \bar{I}_2, \ \bar{I}_3 \end{cases} \tag{14e}$$

$$\text{Fluid}: \begin{cases} M_\infty\dfrac{\hat{h}}{\hat{L}}, \ \mathit{Re}_0 \\ \mathit{Pr}_0, \ \gamma \end{cases} \tag{14f}$$

where,

$$\bar{\lambda}_F = \frac{\gamma p_\infty M_\infty \hat{L}^3}{\widehat{D}_{xx}} \tag{15a}$$

$$\mathit{Bi}_F = \frac{\hat{k}^f}{\hat{k}^s}\mathit{Re}_0\mathit{Pr}_0\frac{\hat{V}^2}{\hat{c}_p^f\hat{T}_T} \tag{15b}$$

Equation (14a) requires the geometric similarity between the model and the prototype, which is easy to satisfy. In Eq. (14b), the three quantities provide conflicting requirements for the time scale, which can be reconciled depending on the type of problem. For example, to simulate long-term quasi-steady aerothermoelastic response, the first parameter representing the thermal characteristic time should be used to define the time scale, and the other two can be ignored.

Equation (14c) provides a group of similarity parameters related to the aerothermoelastic coupling. In the *first row*, the first parameter $\bar{\lambda}_F$ is the nondimensional dynamic pressure, representing the ratio of aerodynamic pressure and the bending stiffness. The second parameter $\mathit{Bi}_F$ is the Biot number associated with the aerodynamic heat flux. The third parameter defines the magnitude of surface deformation, which is important when the panel undergoes moderate deformations. The last four parameters provide the requirements for the reference temperatures in the thermal, structural and fluid problems. The *second row* represents the requirements for the similarity in the distributions of the aerodynamic pressure and heat flux, surface deformation, wall temperature and body temperature. These requirements are automatically satisfied if all other similarity requirements are satisfied.

The parameters in Eqs. (14d)-(14f) are the similarity requirements for the individual disciplines. In each group, the *second row* represents the similarity requirements for material properties as a function of temperature. These requirements are approximately satisfied if the functions representing the temperature dependency of the material properties have a similar form. One example is the case where the material properties of the model and the prototype are proportional to the power of temperature $T^\eta$ over the temperature range of interest, where the exponent $\eta$ is curve-fitted from the material data [7]. The similarity requirements for the temperature-dependent material properties are approximately satisfied, if the difference between the values of $\eta$ associated with the model and the prototype are sufficiently small.

In Eq. (14d), the first parameter, which requires the similarity in the initial temperature distribution, is easy to satisfy. The next two parameters represent the magnitude and distribution of the heat flux due to external heat source, which will be discussed later in this study. In Eq. (14e), first five parameters provide the similarity requirements in various stiffness constants. The parameters associated with $\widehat{B}_{xx}$, $\widehat{S}_{xx}$ and $\widehat{M}_{Tx}$ may be ignored if the panel is orthotropic and sufficiently thin. The last two parameters, which define the magnitude and distribution of the externally-applied loading, will be discussed later. In Eq. (14f), the first parameter may be disregarded due to Mach number independence principle. The second parameter, the Reynolds number, governs the growth of the boundary layer and thus the distribution of pressure and heat flux.

Based on the preceeding discussion, for long-term quasi-steady aerothermoelastic response of skin panel, the similarity parameters in Eq. (14) are reduced and replaced by a simplified set given by Eqs. (16a)-(16d),

$$\mathit{Fo} \tag{16a}$$

$$\frac{\hat{h}}{\hat{L}},\ \bar{h},\ \bar{\lambda}_F,\ \mathbf{\mathit{Bi}}_F,\ \mathbf{\mathit{Re}}_0,\ \frac{\widehat{A}_{xx}\hat{L}^2}{\widehat{D}_{xx}},\ \frac{\widehat{N}_{Tx}\hat{L}^2}{\widehat{D}_{xx}} \tag{16b}$$

$$\frac{T_w}{\hat{T}_S},\ \frac{\hat{T}_T}{\hat{T}_S},\ \frac{T_0}{\hat{T}_S},\ \frac{\hat{T}_F}{\hat{T}_S} \tag{16c}$$

$$\mathbf{\mathit{Bi}}_{ext},\ \bar{\dot{q}}_{ext},\ \bar{\lambda}_{ext},\ \bar{p}_{ext} \tag{16d}$$

## 2.5 Limitations of Complete Aerothermoelastic Scaling

The complete aerothermoelastic scaling requires that (1) all the similarity parameters in Eqs. (16b) and (16c) should be satisfied, and (2) the external loading and heating in Eq. (16d) is zero. Complete aerothermoelastic scaling cannot be achieved due to the conflict between the similarity requirements for the aeroelastic and the aerothermal responses, or specifically, structural stiffness and aerodynamic heating.

First, the quantities $\widehat{A}_{xx}$, $\widehat{N}_{Tx}$, and $\widehat{D}_{xx}$ are functions of the reference structural temperature $\hat{T}_S$. Therefore, from the similarity parameters $\frac{\widehat{A}_{xx}\hat{L}^2}{\widehat{D}_{xx}}$ and $\frac{\widehat{N}_{Tx}\hat{L}^2}{\widehat{D}_{xx}}$, $\hat{T}_S$ is determined. Next, the quantities $\bar{\lambda}_F$, $\mathbf{\mathit{Re}}_0$, and $\mathbf{\mathit{Bi}}_F$ are functions of the flow conditions $p_\infty$, $M_\infty$ and $T_\infty$. Therefore, the flow conditions that satisfies aeroelastic similarity is determined from the combination of $\hat{T}_S$ and parameters $\bar{\lambda}_F$, $\mathbf{\mathit{Re}}_0$ and $\frac{T_0}{\hat{T}_S}$. However, a different set of flow conditions $p_\infty$, $M_\infty$ and $T_\infty$ that satisfies aerothermal similarity is determined from the combination of $\hat{T}_S$ and parameters $\bar{\lambda}_F$, $\mathbf{\mathit{Bi}}_F$ and $\frac{\hat{T}_T}{\hat{T}_S}$. In general, the two sets of flow conditions are not the same and thus complete aerothermoelastic scaling fails.

### 2.6 Strategies for Refined Aerothermoelastic Scaling

The previous discussion has shown that it is impossible to develop a scaled model that satisfies all the aerothermoelastic similarity parameters in Eq. (14) or Eq. (16). However, various *ad hoc* assumptions can be introduced to facilitate the analytical derivation of the similarity parameters. Some complex but important factors in the aerothermoelastic problem have been ignored, including the turbulence and real gas effect in the fluid problem, geometric nonlinearity in the structural problem and the material nonlinearity in the structural and thermal problems. Therefore, while the similarity parameters derived using the classical approach provide useful information about aerothermoelastic scaling, they fail to accurately represent the requirements for constructing aerothermoelastically scaled models.

A refined aerothermoelastic scaling approach is developed in this study to reconcile the conflict that arises in conventional aerothermoelastic scaling, thus overcoming the limitations of the classical scaling approach. Instead of satisfying the aerothermoelastic similarity parameters, the scaled model is constructed by satisfying the similarity in the aerothermoelastic *response*, i.e. minimize the differences between the nondimensional aerothermoelastic responses of the prototype and the model. The aerothermoelastic responses generated using numerical simulation take account of all the complex factors that are ignored in the classical approach. As noted earlier in this section, in this study, the aerothermoelastic responses refer to the time history of the structural deformation and the body temperature in the structure.

Two strategies can be employed in refined aerothermoelastic scaling:

1. *Parameter relaxation*: the scaled model is constructed so as to achieve approximate similarity in the aerothermoelastic responses, while matching a *partial* set of the aerothermoelastic similarity parameters between the prototype and the model, so as to produce the best fit agreement for all the aerothermoelastic similarity parameters.
2. *Incomplete testing*: represents a situation where external loading and heating is introduced in the wind tunnel test to compensate for the differences in the similarity parameters $\bar{\lambda}_F, Bi_F$ associated with the prototype and the model.

Both strategies are difficult to apply to the construction of the scaled model if the classical approach is used alone. However, the two strategies can be combined with the two-pronged approach to enable systematic model adjustment with the objective of achieving aerothermoelastic similarity. The process of model adjustment can be formulated as an optimization problem. The design variables are selected to correspond to the most important parameters needed for the refined simulation, and these design variables differ from those employed when generating the model based on classical similarity. Eventually, the numerical scaling law for the specialized cases can be obtained without recourse to the *ad hoc* assumptions used in the classical approach. Thus, the difficulties associated with hypersonic aerothermoelastic testing are resolved.

The selection of the design variables is problem-dependent. Typically, the design variables should include the freestream flow conditions in the wind tunnel, which cannot be determined using the classical approach due to the conflict between the aeroelastic and aerothermal similarity requirements. For a skin panel configuration, the design variables should also include the geometrical parameters of the scaled model, such as the panel thickness and the side length. The classical approach requires all the geometrical parameters to scale uniformly using the same scaling factor. However, it could be advantageous to scale the geometrical parameters using different scaling factors so as to achieve a better agreement between the nondimentional aerothermoelastic response of the prototype and the model [19].

## 3 OVERVIEW OF THE COMPUTATIONAL FRAMEWORK

The computational tools required for the right-hand branch of the two-pronged approach are derived from the computational framework denoted HYPATE, HYPersonic AeroThermoElasticity simulation environment, developed in our previous studies [21, 30, 31]. The code structure of the HYPATE framework is illustrated in Fig. 5. The framework employs a partitioned approach using a loosely-coupled or a tightly-coupled scheme. The fluid, thermal and structural responses are computed by separate solvers and the coupling is achieved by exchanging boundary data at the interfaces of the physical domains. Moreover, a solver based on linearized stability analysis (LSA) is developed as an extension of the $p$-method in aeroelasticity [19, 32]. The LSA is employed to examine the stability of the deformed structure at every time step, so as to detect the onset of aerothermoelastic instability.

The loosely-coupled and the tightly-coupled schemes are illustrated in Figs. 6 and 7. The loosely-coupled scheme is efficient for obtaining the general transient aerothermoelastic response, since the boundary data is exchanged only once between the solvers at each time step. The tightly-coupled scheme is developed for quasi-steady aerothermoelastic response prior to the onset of instability. The fluid and the structural domains are solved simultaneously at each time step. This approach allows 1-2 order of magnitude larger time step size when compared to the loosely-coupled scheme. Therefore, the tightly-coupled scheme is employed for generating long-term quasi-steady aerothermoelastic responses.

The structural and thermal solvers are based on a parallel C++ library with Python interface developed for general finite element analysis [31]. The structural solver is capable of modeling the structural dynamics of anisotropic doubly curved shallow shells, with shear, geometric nonlinearity and thermal stress. The thermal solver models heat transfer in composite shells using layer-wise thermal lamination theory. Both solvers account for temperature-dependent material properties.

The HYPATE framework contains fluid solvers having different levels of fidelity. The low-fidelity fluid solver is based on analytical models. The aerodynamic pressure is computed using piston theory [33] and the heat flux is computed using Eckert's reference method [34]. The low-fidelity fluid solver has been used to verify the correctness of the code implementation of the framework in the previous studies [31]. The high-fidelity fluid solver is the CFD solver, Automatic Differentiation flow solver (ADflow) [35, 36]. The ADflow code is a highly-parallelized, multiblock, finite volume solver based on Reynolds-Averaged Navier-Stokes (RANS) equations. The Arbitrary Lagrangian-Eulerian formulation is implemented in ADflow for problems with moving boundary [31]. The Spalart-Allmaras turbulence model and perfect gas model are employed for hypersonic aerodynamic computation.

The use of the CFD solver is limited due to its high computational cost while the low-fidelity fluid solver fails to capture the complex flow physics associated with hypersonic flow. Therefore, reduced-order modeling (ROM) techniques are applied to accelerate the CFD fluid solver in the HYPATE framework [21, 30]. The ROM takes advantage of the quasi-steady nature of the hypersonic flow, i.e. the disparity of characteristic times of different physical domains: The fluid characteristic time is several orders of magnitude smaller than the structural characteristic time, and the structural characteristic time is several orders of magnitude smaller than the thermal characteristic time [24]. Therefore, in the ROM, the aerodynamic loading is modeled by combining a steady fluid solution with an unsteady contribution generated by piston theory. The steady fluid solution is modeled using the kriging method and proper orthogonal decomposition (POD), namely the POD-kriging method [37–39]. By using the ROM, the fluid solver is accelerated by five orders of magnitude for skin panel applications, while maintaining the accuracy of a CFD solver [21, 30].

A conventional ROM based on the POD-kriging method is only applicable to a fixed geometrical configuration and cannot be used to predict the aerodynamic loading and heating of a different configuration. In Refs. [19–21], a ROM correction and scaling technique was developed to enable the extrapolation of *one* ROM to different geometrical scales and flight conditions. The corrected and scaled ROM permits the conduction of an extensive parametric study of numerical aerothermoelastic solutions for different scales of geometric configurations and different combinations of flight conditions that are required in the optimization process of the two-pronged approach.

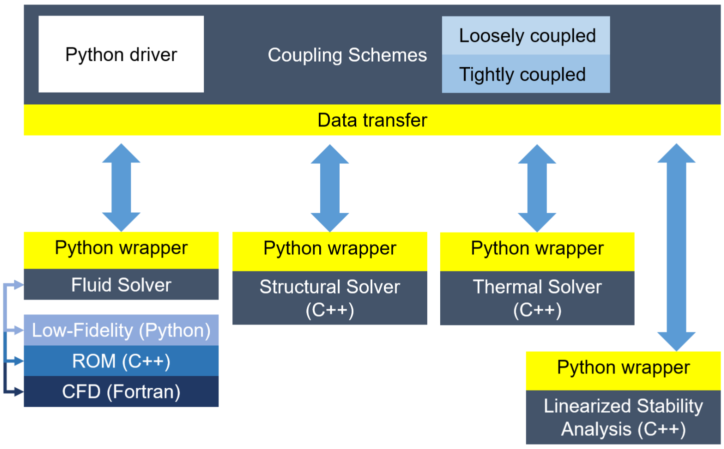

Figure 5: Code structure of the extended HYPATE framework.

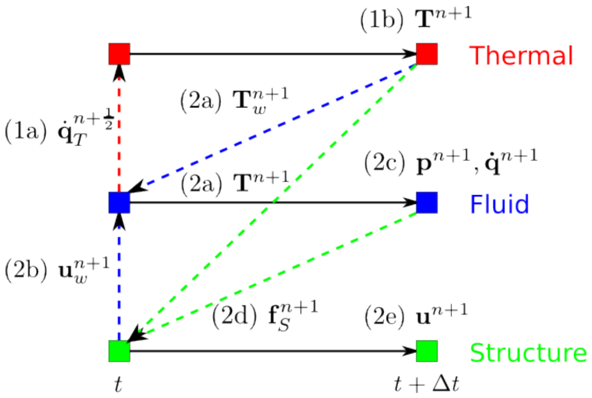

Figure 6: Loosely-coupled scheme.

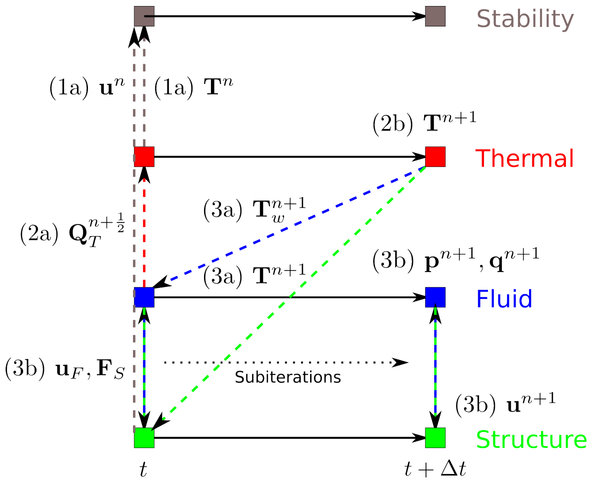

Figure 7: Tightly-coupled scheme.

# 4 OPTIMIZATION FORMULATION FOR THE TWO-PRONGED APPROACH

## 4.1 Objectives

The two-pronged approach combines the classical dimensional analysis and the numerical simulation method to systematically adjust the wind tunel model properties so as to enable hypersonic aerothermoelastic testing. For a generic configuration, the adjustment process is formulated as a constrained optimization problem that searches for a wind tunnel setup whose aerothermoelastic response could represent that of the full-scale prototype to the largest extent possible. The aerothermoelastic responses of the prototype and the model are computed using the HYPATE framework. The simulated aerothermoelastic response of the prototype is a time history of deformation and body temperature. The similarity of the solutions is measured using two objective functions, representing the differences between the nondimensional solutions to be minimized. For the deformation and temperature, the objective functions are defined, respectively, as:

$$J_u(\mathbf{d}; \{\mathbf{u}_i^m\}) = \sqrt{\sum_{i=1}^{N_t} \left\| \mathbf{\Psi}_u^T \left( \frac{\mathbf{u}_i^m}{\hat{u}^m} - \frac{\mathbf{u}_i^p}{\hat{u}^p} \right) \right\|^2} \tag{17a}$$

$$J_T(\mathbf{d}; \{\mathbf{T}_i^m\}) = \sqrt{\sum_{i=1}^{N_t} \left\| \mathbf{\Psi}_T^T \left( \frac{\mathbf{T}_i^m}{\hat{T}^m} - \frac{\mathbf{T}_i^p}{\hat{T}^p} \right) \right\|^2} \tag{17b}$$

where $\mathbf{d}$ is the vector of design variables. The projection matrices $\mathbf{\Psi}_u$ and $\mathbf{\Psi}_T$ converts the full aerothermoelastic responses to the quantities of interest, such as the modal components of the deformation and temperature.

The objectives are meaningful only when the differences between the nondimensional solutions are computed at the *same* nondimensional time. The matching of the nondimensional time is guaranteed by using the same nondimensional time step size for the prototype and the model. In other words, the time step size of the model $\Delta t^m$ should be determined from the time step size of the prototype $\Delta t^p$ by keeping one of the similarity parameters in Eq. (14b) constant. For example, for the case of long-term quasi-steady aerothermoelastic response, given $\Delta t^p$, the time step size $\Delta t^m$ should be determined such that the Fourier numbers of the model and the prototype are the same,

$$\frac{[\hat{k}^s]^m \Delta t^m}{[\hat{\rho}^s \hat{c}_p^s]^m (\hat{h}^m)^2} = \frac{[\hat{k}^s]^p \Delta t^p}{[\hat{\rho}^s \hat{c}_p^s]^p (\hat{h}^p)^2} \quad \Rightarrow \quad \Delta t^m = \frac{[\hat{k}^s]^p [\hat{\rho}^s \hat{c}_p^s]^m}{[\hat{k}^s]^m [\hat{\rho}^s \hat{c}_p^s]^p} \left( \frac{\hat{h}^m}{\hat{h}^p} \right)^2 \Delta t^p \tag{18}$$

## 4.2 Design Variables and Constraints

For the case of skin panel, the design variables describing the full-scale prototype and the wind tunnel test model are summarized in Table 1. Note that external loading is introduced by $p_{ext}$ and external heating is introduced by radiant heating specified by the radiation temperature $T_{rad}$ and the surface emissivity $\varepsilon$ [40]. Not all of the variables in the wind tunnel setup are continuous. First, in most hypersonic wind tunnels, the *freestream* flow conditions are given as constant, or can be selected from a very limited number of discrete options provided by using different nozzle configurations. Second, due to high loads and temperatures during aerothermoelastic testing, there are only a limited number of options for material properties, i.e. elastic constants $\mathbf{Q}$, thermal expansion coefficients $\boldsymbol{\alpha}$ and thermal properties $\mathbf{k}^s$ and $c_p^s$. Nevertheless, some wind

Table 1: Design variables for the optimization problem

| Group | Design variables | Type | Lower limits | Upper limits |
|---|---|---|---|---|
| Flow conditions | $M_\infty$ | Disc. | N/A | |
| | $p_0, T_0$ | Cont. | Wind tunnel | |
| Geometry | $\hat{L}, L_{le}, \theta$ | Cont. | Manufacture | Wind tunnel |
| Composite layup | $\mathbf{Q}, \boldsymbol{\alpha}, \mathbf{k}^s, c_p^s$ | Disc. | N/A | |
| | $\mathbf{h}$ | Cont. | Manufacture | Wind tunnel |
| External loading | $p_{ext}$ | Cont. | Wind tunnel | |
| | $T_{rad}$ | Cont. | Wind tunnel | |
| | $\varepsilon$ | Cont. | 0 | 1 |
| Temperatures | $\hat{T}_T, \hat{T}_S$ | Cont. | Arbitrary | |
| | $T_w$ | Cont. | Wind tunnel | |

tunnels do have the capability to adjust the stagnation temperature and pressure continuously [17]. Moverover, a continous range of *post-shock* flow conditions can be achieved by adjusting the geometrical inclination angle $\theta$ of the panel. Furthermore, the thickness of each lamina may be adjusted to tune the structural and thermal properties of the model. Finally, it is assumed that a continous range of the surface emissivity $\varepsilon$ can be achieved by applying different coating to the surface of the scaled model, so as to adjust the magnitude of the radiative heat flux acting on the model.

Based on preceeding discussion, the design variables are divided into two groups,

$$\mathbf{d}_c = [p_0, T_0, \hat{L}, L_{le}, \theta, \mathbf{h}, p_{ext}, T_{rad}, \varepsilon, \hat{T}_T, \hat{T}_S, T_w] \tag{19a}$$

$$\mathbf{d}_d = [M_\infty, \mathbf{Q}, \boldsymbol{\alpha}, \mathbf{k}^s, c_p^s] \tag{19b}$$

where $\mathbf{d}_c$ and $\mathbf{d}_d$ are the vectors of the continuous and discrete design variables, respectively.

The design variables have to satisfy two sets of constraints, the equality and the inequality ones. The equality constraints are due to the requirement that the similarity parameters of the model and the prototype should be equal. When the parameter relaxation or incomplete testing strategy is employed, not all similarity parameters in Eqs. (16b) and (16c) are used as equality constraints. For example, the heat flux parameter $Bi_F$ is excluded from the equality constraints if external heating is provided. The inequality constraints are due to practical limits and the factors characterizing the lower and upper limits of the inequality constraints are summarized in the last two columns of Table 1. The lower and upper limits of the geometrical quantities are determined by the limitations in model manufacture and the size of the wind tunnel, respectively. The feasible ranges of external loading and temperature are determined by the capabilities of the wind tunnel facility.

### 4.3 Formulation of Optimization Problem

Combining Eqs. (17) and (19), the two-pronged approach for refined scaling law is formulated as a constrained Multi-objective Optimization (MO) problem,

$$\text{Minimize} \quad \mathbf{J}(\mathbf{d}_c, \mathbf{d}_d) = [J_u(\mathbf{d}_c, \mathbf{d}_d), J_T(\mathbf{d}_c, \mathbf{d}_d)] \tag{20a}$$

$$\text{Subject to} \quad \mathbf{c}_E(\mathbf{d}_c, \mathbf{d}_d) = 0 \tag{20b}$$

$$\mathbf{c}_I(\mathbf{d}_c, \mathbf{d}_d) \leq 0 \tag{20c}$$

where Eqs. (20b) and (20c) represent the equality and inequality constraints, respectively. The optimization problem Eq. (20) is a mixed-integer optimization problem that is difficult to solve, due to the presence of both continuous and discrete design variables. However, since there is only a limited number of feasible values for the discrete design variables, the full problem Eq. (20) can be solved by an exhaustive search on all feasible values for $\mathbf{d}_d$. For each possible set of $\mathbf{d}_d$, the optimal solution is found by solving the continuous optimization problem w.r.t. $\mathbf{d}_c$,

$$\begin{aligned} \text{Minimize} \quad & \mathbf{J}(\mathbf{d}) = [J_u(\mathbf{d}), J_T(\mathbf{d})] && \text{(21a)} \\ \text{Subject to} \quad & \mathbf{c}_E(\mathbf{d}) = 0 && \text{(21b)} \\ & \mathbf{c}_I(\mathbf{d}) \leq 0 && \text{(21c)} \end{aligned}$$

where the subscript $c$ of $\mathbf{d}_c$ is dropped for convenience.

## 5 SOLUTION STRATEGIES FOR THE MO PROBLEM

An MO problem typically has multiple solutions. Each solution of an MO problem is Pareto optimal, meaning that one objective cannot be decreased without increasing the other objectives. The set of all the Pareto optimal solutions is called the Pareto front $\mathcal{F}$. A typical pareto front for a two-objective optimization problem is illustrated in Fig. 8. The gray shaded area represents the solution space, which is the set of all possible combinations of the objective values. At points $A$ and $D$, the objectives $J_u$ and $J_T$ achieve the minimum possible values in the solution space, respectively. The Pareto front is the subset of the boundary of the solution space between points $A$ and $D$, represented by solid black curves. Note that the continuity of the Pareto front is not a requirement. In Fig. 8, Point $B$ represents a combination of objectives in the solution space that is better than any point on the gray curve $BC$. As a result, the Pareto front is disconnected and consists of only the curves $AB$ and $CD$, and not the curve $BC$. While multiple solutions are possible, the ultimate goal is to identify *one* optimal solution from the Pareto front, referred to as the *design point* in the following discussion. The design point represents a wind tunnel configuration that minimizes the differences in the nondimensional aerothermoelastic responses of the prototype and the model.

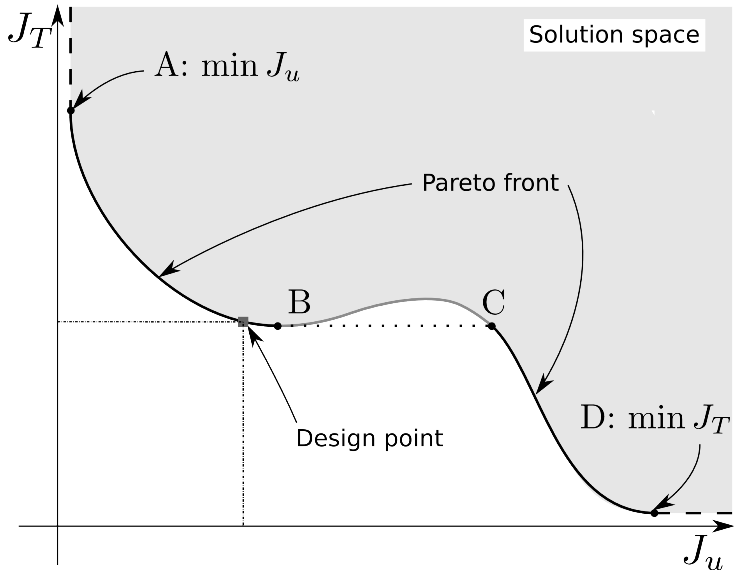

Figure 8: Illustration of a typical Pareto front of a two-objective problem

An additional challenge associated with the MO problem Eq. (21) is the expensive computational cost of the objectives, due to the aerothermoelastic simulation over the extended flight time. To solve the MO problem within a practical amount of time, the number of evaluations of the objectives has to be limited during optimization. As a result, there are two limitations on the optimization algorithm: (1) The design space cannot be explored by carrying out numerous *direct* evaluation of the objectives; (2) The derivative of the objectives w.r.t. design variables cannot be computed using the finite difference approach. To overcome the two limitations, the Surrogate-Based Optimization (SBO) algorithm is employed in the current study [41]. Using the SBO algorithm, two approaches are employed to find the design point associated with the MO problem. The indirect approach produces a Pareto set $\overline{\mathcal{F}}$, i.e. a set of Pareto optimal solutions, that is representative of the Pareto front $\mathcal{F}$. The design point has to be selected from the Pareto set manually by the user. The direct approach does not produce a Pareto set. Instead, it only generates one Pareto optimal solution, identified as the design point.

In the rest of this section, the general procedure of the SBO algorithm is provided first. Next, the direct and indirect approaches using the SBO algorithm are presented and compared. Finally, the implementation details of the optimization algorithms are discussed.

### 5.1 Surrogate-Based Optimization

The SBO algorithms contain two key ingredients, a surrogate model and an acquisition function. The surrogate model is employed to approximate the expensive objectives. Since the surrogate is computationally efficient, it allows the fast evaluation of approximated objectives as well as its derivative w.r.t. the design variables. The acquisition function is a criterion for selecting the points in the design space that is potentially a solution to the optimization problem. It is designed to take into account two ingredients, namely *exploration*, i.e. sampling from areas of high uncertainty, and *exploitation*, i.e. sampling from areas likely to improve the objectives. A typical SBO algorithm contains the following steps,

1. Set the number of initial samples $N_s$, number of iterations $N_i$.
2. Generate initial sample points $\{\mathbf{d}_i\}_{i=1}^{N_s}$ in the design space using a sampling approach, e.g. the Optimial Latin Hypercube (OLH) method [41].
3. Generate a sample data set $\mathcal{D} = \{(\mathbf{d}_i, \mathbf{J}_i, \mathbf{c}_{Ei}, \mathbf{c}_{Ii})\}_{i=1}^{N_s}$ by evaluating the objectives and constraints $\mathbf{J}_i, \mathbf{c}_{Ei}, \mathbf{c}_{Ii}$ at the initial sample points.
4. Inner optimization for a maximum of $N_i$ iterations:
   (a) Generate surrogates $\mathbf{J}^{sur}(\mathbf{d})$, $\mathbf{c}_E^{sur}(\mathbf{d})$, $\mathbf{c}_I^{sur}(\mathbf{d})$ for the objectives and constraints using the sample data set $\mathcal{D}$.
   (b) Find the candidate point $\mathbf{d}^*$ by solving an optimization problem that consists of the surrogates and acquisition function.
   (c) Evaluate the objective and constraint functions $\mathbf{J}_i^*, \mathbf{c}_{Ei}^*, \mathbf{c}_{Ii}^*$ at the candidate point $\mathbf{d}^*$.
   (d) Update the surrogate using the sample data set augmented with the candidate solution $\mathcal{D}^* = \mathcal{D} \cup \{(\mathbf{d}^*, \mathbf{J}^*, \mathbf{c}_E^*, \mathbf{c}_I^*)\}$.
   (e) Break if convergence criteria is met, otherwise continue.

The SBO algorithms are classified in two categories: the one-shot approach and the updating approach [42]. The one-shot approach only excutes the inner optimization step once. The candidate solution is accepted as the final solution regardless of the differences between the surrogate and the objectives at the candidate point. The one-shot approach might fail if the design space is not well represented by the sample data set and the uncertainty of the surrogate at the candidate point is high. In the updating approach, the inner optimization is executed until convergence or when the computational budget is exceeded. While the updating approach does not guarantee finding the global optimum point, it usually produces a better solution than the one-shot approach [42,43]. In this study, the updating approach is employed.

Several surrogate models have been employed in SBO algorithms, e.g. response surfaces [44] and the kriging method [42,43,45]. The kriging method, or the Gaussian process regression model [46], is employed for SBO in this study, because it has a clear statistical interpretation that is beneficial in the construction of acquisition functions. The prediction of the kriging model at a candidate point $\mathbf{d}^*$ follows a joint Gaussian probability distribution,

$$\mathbf{J}^* = \mathbf{J}^{sur}(\mathbf{d}^*) \sim \mathcal{N}(\boldsymbol{\mu}(\mathbf{d}^*), \boldsymbol{\Sigma}(\mathbf{d}^*)) \tag{22}$$

where $\boldsymbol{\mu}$ is the predicted values of objectives and $\boldsymbol{\Sigma}$ is the covariance matrix quantifying the uncertainty of the prediction. The objectives are assumed to be independent and thus $\boldsymbol{\Sigma}$ is a diagonal matrix. The standard deviations associated with the predicted values are denoted as $\boldsymbol{\sigma}$.

Note that the updating SBO algorithms using kriging method appear in the literature under multiple names, such as Efficient Global Optimization (EGO) [43,45] and Bayesian Optimization (BO) [47,48]. Throughout the rest of the paper, the updating SBO algorithms is referred to as "Bayesian optimization", due to its statistical interpretation.

## 5.2 Multi-Objective Optimization Using the BO Algorithm

### *5.2.1 Direct Approach*

In the direct approach, the MO problem is reformulated as a Single-objective Optimization (SO) problem and the design point is found by solving the SO problem only once,

$$\begin{aligned} \text{Minimize} \quad & J_s(\mathbf{d}) = \mathcal{S}(\mathbf{J}(\mathbf{d})) && \text{(23a)} \\ \text{Subject to} \quad & \mathbf{c}_E(\mathbf{d}) = 0 && \text{(23b)} \\ & \mathbf{c}_I(\mathbf{d}) \leq 0 && \text{(23c)} \end{aligned}$$

where a function $\mathcal{S}(\mathbf{J})$ is introduced to combine the vector of objectives into a scalar objective, typically using a Weighted Metric (WM) method. For the MO problem Eq. (21), the objectives $J_u$ and $J_T$ are combined as,

$$\mathcal{S}_g(\mathbf{J}) = [(c_u J_u)^g + (c_T J_T)^g]^{1/g} \tag{24}$$

where $g \in [1, \infty]$ and $0 \leq c_u, c_T \leq 1$. The weights $c_u, c_T$ are determined empirically and more emphasis is placed on the objective with the larger weight.

Two special cases of WM method are illustrated in Figs. 9(a) and 9(b). The first special case is the WM method with $g = 1$, which is equivalent to the weighted sum method [49],

$$\mathcal{S}_1(\mathbf{J}) = c_u J_u + c_T J_T \tag{25}$$

A Pareto optimal solution found by the weighted sum method is illustrated by the point $E$ in Fig. 9(a). The contours of the combined objective $\mathcal{S}_1(\mathbf{J})$ are a family of straight lines of slope $-\frac{c_u}{c_T}$. The weighted sum method finds the point at which the contour of $\mathcal{S}_1$ is tangent to the Pareto front and the contour does not intersect with the rest of the solution space. However, the weighted sum method can only find points on a partial set of a non-convex Pareto front. At point $F$ of the Pareto front in Fig. 9(a), it is impossible to find a contour of $\mathcal{S}_1$ at $F$ that does not intersect with the solution space.

The second special case is the WM method with $g = \infty$, where the objectives are combined as,

$$\mathcal{S}_\infty(\mathbf{J}) = \max(c_u J_u, c_T J_T) \tag{26}$$

The WM method with $g = \infty$ is capable of finding all the Pareto points on the Pareto front and its geometrical interpretation is provided in Fig. 9(b). The contours of the combined objective $\mathcal{S}_\infty(\mathbf{J})$ are a family of rectangles whose diagonals have a slope of $\frac{c_T}{c_u}$. The WM method with $g = \infty$ finds the point that is the only intersection between a contour of $\mathcal{S}_\infty$ and the solution space. The point is either the tangent point between the contour and the Pareto front, such as point $B$, or the corner point of the contour, such as point $F$.

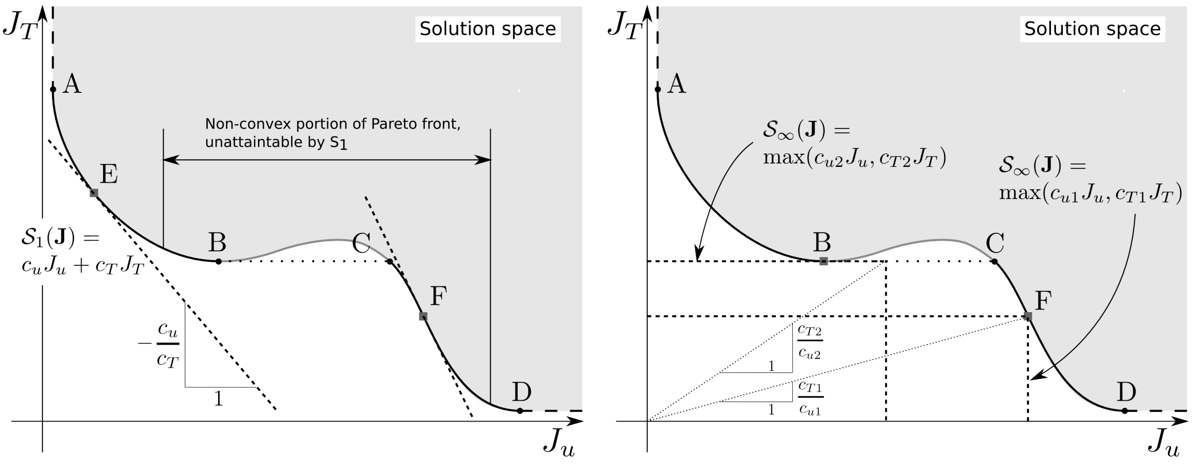

**(a) Weighted metric with $g = 1$, i.e. weighted sum method**

**(b) Weighted metric with $g = \infty$**

Figure 9: Illustration of two typical WM methods

Surveys of acquisition functions for SO problems can be found in, for example, Refs. [45] and [50]. There are three basic acquisition functions: (1) Probability of Improvement (PoI) [51], (2) Expected Improvement (EI) [47,52], (3) Lower Confidence Bound (LCB) [53]. The formulation of these acquisition functions is presented next.

**Probability of Improvement.** The PoI acquisition function is defined as the probability of the new design point $\mathbf{d}^*$ that represents a better value of the objective $J^*$ when compared to the minimum objective in the sample data set $J_{\min} = \min J_i$.

$$C_{PoI}(\mathbf{d}^*) = P(J^* \leq J_{\min}) = 1 - \Phi(z_0) \tag{27}$$

where $z_0 = \frac{J_{\min} - \mu}{\sigma}$ and $\Phi$ is the cummulative distribution function of a standard Gaussian distribution.

**Expected Improvement.** The EI acquisition function is defined as the expectation of the improvement in the objective at the new design point. In the literature, EI has been generalized to include user-specified parameters that control the exploitation-exploration trade-off. The generalized EI is written as [52],

$$C_{EI}(\mathbf{d}^*) = \mathbb{E}[\mathcal{I}(\mathbf{d}^*)] \tag{28}$$

where $\upsilon \geq 0$ and $g \geq 1$ are the user-specified parameters, and

$$\mathcal{I}(\mathbf{d}) = \max(0, (J_{\min} - J^{sur}(\mathbf{d}) - \upsilon\sigma(\mathbf{d}))^g) \tag{29}$$

A larger $g$ or $\upsilon$ will put more weight on the exploration. The classical form of EI is obtained with $\upsilon = 0$ and $g = 1$. When $\upsilon > 0$ and $g = 1$, the EI is equivalent to the weighted EI function developed in Ref. [42]. When $\upsilon = 0$ and $g = 0$, EI reduces to PoI. For a kriging model, the closed-form expression is available for $C_{EI}$. For the case $g = 1$,

$$C_{EI}(\mathbf{d}^*) = \int_0^\infty \mathcal{I} P(J^{sur} = J_{\min} - \upsilon\sigma - \mathcal{I})\mathrm{d}\mathcal{I} \tag{30}$$

$$= \begin{cases} \sigma[z\Phi(z) + \phi(z)], & \sigma > 0 \\ 0, & \sigma = 0 \end{cases} \tag{31}$$

where $z = \frac{J_{\min} - \upsilon\sigma - \mu}{\sigma}$.

**Lower Confidence Bound.** The LCB acquisition function is defined using the LCB concept of a Gaussian probability distribution,

$$C_{LCB}(\mathbf{d}^*) = \mu(\mathbf{d}^*) - \upsilon\sigma(\mathbf{d}^*) \tag{32}$$

where the probability of $J^{sur} < C_{LCB}$ is a constant controlled by the user-specified parameter $\upsilon > 0$. A larger $\upsilon$ will put more weight on the exploration.

The PoI acquisition function is purely exploitation, which is undesirable for global optimization. The EI and LCB acquisition functions are high when $J^*$ approaches the optimum point, or the uncertainty of $J^*$ is high. Therefore, both $C_{EI}$ and $C_{LCB}$ achieve a balance between exploitation and exploration. The LCB function is smoother than the EI function and thus more favorable for the inner optimization of the BO algorithm. Therefore, the LCB function is employed in the current study.

Finally, note that the exploitation-exploration trade-off of EI and LCB functions can be further tuned by a cooling scheme. In the cooling scheme, the optimization starts with a large user-specified parameter $\upsilon$ for more exploration and gradually decreases the parameter to focus on exploitation. However, the effect of this scheme is controversial [45, 54], and not employed in the study.

### *5.2.2 Indirect Approach*

In the indirect approach, the original MO problem formulation Eq. (21) is retained. The acquisition functions suitable for multiple objectives are developed, so that each inner optimization step of the BO algorithm produces one Pareto optimal solution of the MO problem. The optimization algorithm generates a Pareto set and the user needs to select one of the Pareto optimal solutions as the final design point.

The PoI, EI and LCB acquisition functions for SO problems have been extended to MO problems using the concept of hypervolume (HV), denoted by $\mathcal{H}$ [55–57]. Figure 10 illustrates the hypervolume associated with a two-objective problem. Initially, the Pareto set $\overline{\mathcal{F}}_1$ consists of three Pareto optimal solutions labelled by the blue dots. All the points in the purple shaded region are worse than one or more solutions in $\overline{\mathcal{F}}_1$ and better than a reference solution labelled by a green square on the top right corner of Fig. 10. The area of the purple shaded region is defined as the hypervolume associated with the Pareto set $\overline{\mathcal{F}}_1$. A new Pareto set $\overline{\mathcal{F}}_2$ is generated by augmenting $\overline{\mathcal{F}}_1$ with a new solution $\mathbf{J}^*$. The hypervolume associated with $\overline{\mathcal{F}}_2$ is larger than $\overline{\mathcal{F}}_1$ due to the additional area introduced by $\mathbf{J}^*$, as represented by the gray rectangle. The area of the gray rectangle is defined as the hypervolume indicator $I_{\mathcal{H}}$, which quantifies the improvement of a Pareto set due to a new solution $\mathbf{J}^*$.

Given a Pareto set $\overline{\mathcal{F}}$ and a new solution $\mathbf{J}^*$, the hypervolume indicator is written as,

$$I_{\mathcal{H}}(\mathbf{J}^*;\overline{\mathcal{F}}) = \mathcal{H}(\overline{\mathcal{F}} \cup \{\mathbf{J}^*\}) - \mathcal{H}(\overline{\mathcal{F}}) \tag{33}$$

When a new solution $\mathbf{J}^*$ fails to improve the existing Pareto set $\overline{\mathcal{F}}$, the hypervolume indicator associated with $\mathbf{J}^*$ is zero,

$$\mathcal{H}(\overline{\mathcal{F}} \cup \{\mathbf{J}^*\}) = \mathcal{H}(\overline{\mathcal{F}}) \quad \Rightarrow \quad I_{\mathcal{H}}(\mathbf{J}^*;\overline{\mathcal{F}}) = 0 \tag{34}$$

which means no improvement to $\overline{\mathcal{F}}$ is introduced by the new solution.

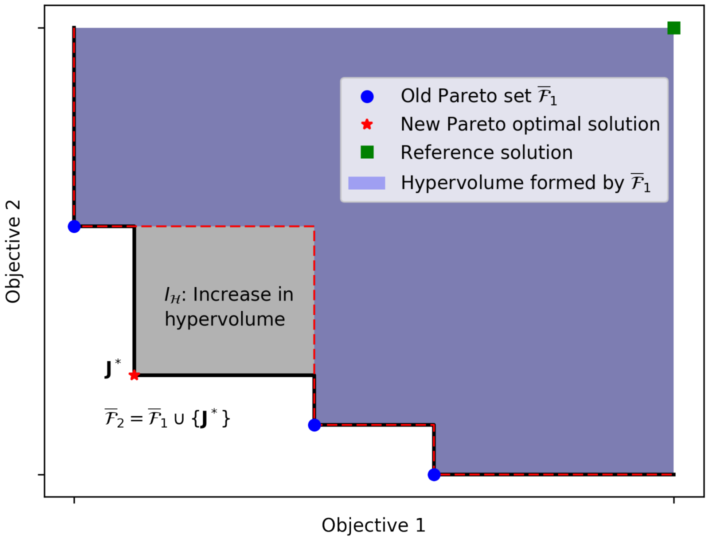

Figure 10: Illustration of the hypervolume indicator

The MO counterparts of the PoI, EI and LCB acquisition functions are defined based on the hypervolume indicator as presented in the following.

**Hypervolume PoI.** The HVPoI acquisition function is developed in Ref. [57], as the hypervolume counterpart of the PoI function. It is defined as follows,

$$C_{HVPoI}(\mathbf{d}) = \int \mathcal{I}(\mathbf{J};\overline{\mathcal{F}}) P(\mathbf{J}^{sur} = \mathbf{J}) \mathrm{d}\mathbf{J} \tag{35}$$

where $\overline{\mathcal{F}}$ is the Pareto set of the current iteration, and

$$\mathcal{I}(\mathbf{J};\overline{\mathcal{F}}) = \begin{cases} 1, & \text{if } I_{\mathcal{H}}(\mathbf{J};\overline{\mathcal{F}}) > 0 \\ 0, & \text{otherwise} \end{cases} \tag{36}$$

**Hypervolume EI.** The HVEI acquisition function is initially proposed under the name “S-metric expected improvement” in Refs. [58, 59] as an extension of the EI acqusition function of SO problems. The formulation is straight-forward by replacing the improvement function in Eq. (30) with the hypervolume indicator,

$$C_{HVEI}(\mathbf{d}) = \int I_{\mathcal{H}}(\mathbf{J};\overline{\mathcal{F}}) P(\mathbf{J}^{sur} = \mathbf{J}) \mathrm{d}\mathbf{J} \tag{37}$$

**Hypervolume LCB.** The HVLCB acquisition function is initially proposed in Ref. [56] as an extension of the LCB acqusition function of SO problems. It was shown to outperform other popular MO algorithms, such as ParEGO [49], NSGA-II [60] and SPEA-2 [61]. This method is easy to implement and has been widely used. Assuming the Pareto set of the current iteration is $\overline{\mathcal{F}}$, the HV counterpart of the LCB function is defined as follows,

$$C_{HVLCB}(\mathbf{d}^*) = \begin{cases} I_{\mathcal{H}}(\mathbf{J}_0; \overline{\mathcal{F}}), & \text{if } I_{\mathcal{H}}(\mathbf{J}; \overline{\mathcal{F}}) > 0 \\ \min\limits_{\mathbf{J} \in \overline{\mathcal{F}}} \left\| \mathbf{J} - \mathbf{J}_0 \right\|, & \text{otherwise} \end{cases} \tag{38}$$

where $\mathbf{J}_0 = \boldsymbol{\mu}(\mathbf{d}^*) - \upsilon \boldsymbol{\sigma}(\mathbf{d}^*)$.

Similar to the discussion in the direct approach, the HVLCB function is employed for the indirect approach due to its smoothness and the exploitation-exploration trade-off property.

### *5.2.3 Comparison of the Direct and Indirect Approaches*

The comparison between the direct and indirect approaches is illustrated in Fig. 11. In the direct approach, the MO problem is reformulated as an SO problem and the design point is found by solving the SO problem only once. The direct approach is employed when there is sufficient preference information on the objectives, i.e. the knowledge about the relative importance of the objectives. The preference information provides the criterion for selecting the weights for objective combination as in Eq. (24). When the MO problem has objectives with limited user knownledge and the weights for objective combination cannot be determined easily, the indirect approach is employed to explore the design space associated with the MO problem. The indirect approach produces a set of representative Pareto optimal solutions and the user needs to manually pick one solution as the design point. In general, the direct approach is preferred whenever it is applicable, because the direct approach only requires solving one optimization problem and generally takes fewer iterations to converge when compared to the indirect approach.

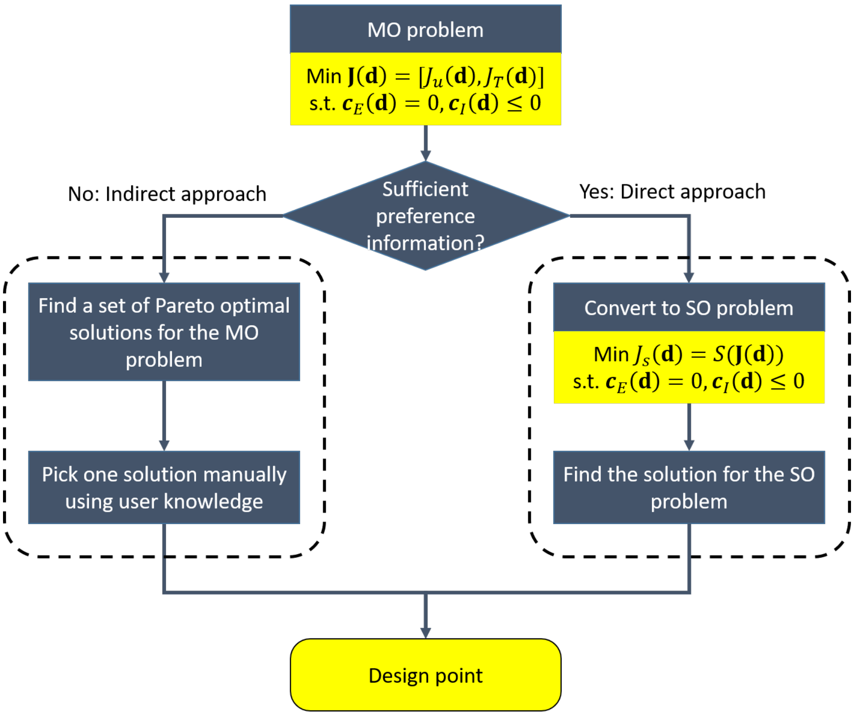

Figure 11: Illustration of direct and indirect approaches for solving the MO problem

## 5.3 Implementation Details

In the current study, both the direct and indirect approaches for the MO problems are implemented in a Python library, Multi-Objective Bayesian Optimization (MOBO), that is developed at the University of Michigan. For the SO problem associated with the direct approach, BO algorithms employing PoI, EI, LCB acquisition functions are implemented. For the indirect approach, BO algorithms employing HVPoI and HVLCB acquisition functions are implemented. The kriging model is generated using the scikit-learn library [62].

No matter which surrogate model and acquisition function are used, eventually the BO algorithm boils down to a series of non-convex subproblems in the inner optimization step. It is hard to find the global optimum of a non-convex function. One choice is to use global optimization algorithms, such as the DIviding RECTangules (DIRECT) algorithm [63]. Another choice is to apply local optimization algorithms, especially the gradient-based algorithms, with multiple starts. In practice, multiple restarts usually result in a good global sub-optimal point that is sufficient for the engineering purposes. Therefore, in the current study, the inner optimization step of the BO algorithm is solved using a gradient-based algorithm, Sequential Least-SQuares Programming (SLSQP), implemented in the SciPy library [64] with multiple starts. The initial starting points are generated using the OLH method at the beginning of every inner optimization step.

## 6 AEROTHERMOELASTIC SCALING OF A SKIN PANEL

The effectiveness of two-pronged approach for generating numerical scaling laws is demonstrated using two cases. In the first case, the two-pronged approach is employed to generate the numerical scaling laws for the transient aeroelastic response of a uniformly heated panel. The aeroelastic case represents a simplified aerothermoelastic problem, for which the analytical scaling laws exist. The first case serves as a sanity check to demonstrate that the two-pronged approach can reproduce the analytical scaling laws via numerical optimization. In the second case, the two-pronged approach is used to develop aerothermoelastically scaled models for a generic panel representing skin of a hypersonic vehicle. This case illustrates the capability for generating numerical hypersonic ASL when considering wind tunnel and manufacturing constraints.

## 6.1 Scaling of Transient Aeroelastic Response

### *6.1.1 Problem Description*

The “prototype” configuration is illustrated in Fig. 12. It consists of a simply-supported square panel with side length of 1 m and thickness of 2 mm. The flight conditions of the prototype are $M_\infty = 6.0$ and $p_\infty = 10^4\mathrm{Pa}$. The flow is aligned with the panel, i.e. the flow orientation angle is zero. Initially, the panel is uniformly heated up by $\Delta T = 1K \approx 2.425T_{cr}$. The aerodynamics is assumed to be inviscid and the piston theory is sufficient for the aeroelastic simulation. The simulation of the prototype is carried out using a time step size of $0.001\mathrm{s}$ to capture the transient aeroelastic response of the panel. The prototype and model panels are made of two different materials Inconel 718 and Ti 6242, respectively, which makes the scaling problem more challenging. The material properties are assumed to be temperature *independent* and equal to the values at room temperature ($T = 300K$) as provided in Table 2. It is also assumed that the Mach numbers and heat capacity ratios associated with the prototype and the model are the same.

Table 2: Material properties of Inconel 718 and Ti 6242 for aeroelastic scaling

| Material | $\rho^s$, $\mathrm{kg/m^3}$ | $E$, GPa | $\nu$ | $\alpha$, $\times 10^{-5}/K$ | $k^s$, $\mathrm{W/m}K$ | $c_p^s$, $\mathrm{J/kg}K$ |
|---|---|---|---|---|---|---|
| Inconel 718 [65] | 8220 | 204.0 | 0.29 | 1.237 | 11.71 | 418.4 |
| Ti 6242 [66] | 4540 | 114.3 | 0.32 | 0.6975 | 6.937 | 459.4 |

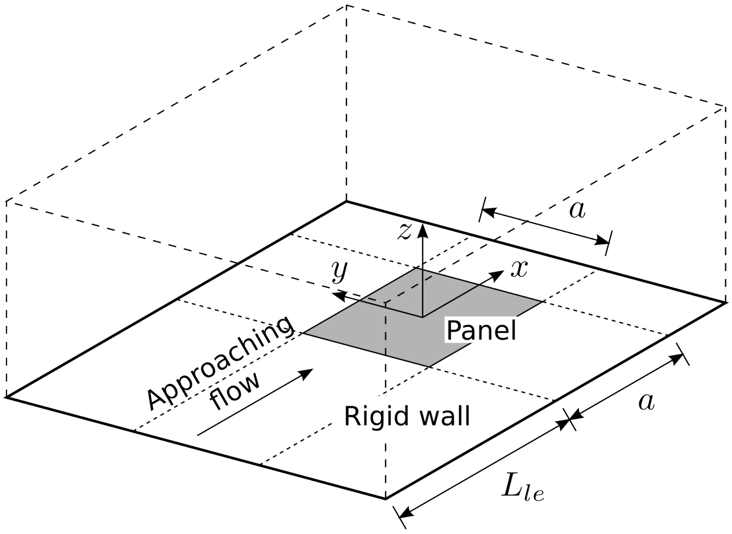

Figure 12: Geometrical configuration of a square panel.

### *6.1.2 Analytical Aeroelastic Similarity Parameters*

Analytical aeroelastic scaling laws exist for a uniformly-heated thin isotropic plate with piston theory aerodynamics, involving the similarity parameters (pp. 85-88 of Ref. [67]),

$$\frac{\hat{h}}{\hat{L}}, \bar{\lambda}_F, \frac{\Delta\hat{T}\widehat{N}_{Tx}\hat{L}^2}{\widehat{D}_{xx}} \tag{39a}$$

$$\frac{\hat{I}\hat{L}^4}{\widehat{D}_{xx}\hat{t}^2} \tag{39b}$$

When the dimension of the scaled model $L^m$ is given, the geometric scale ratio $\xi = \frac{L^p}{L^m}$, and the panel thickness, freestream pressure, and temperature increment associated with the scaled model are determined using Eq. (39a) as follows,

$$h^m = \frac{1}{\xi}h^p \tag{40a}$$

$$p_\infty^m = \xi^3 \frac{\widehat{D}_{xx}^m}{\widehat{D}_{xx}^p} p_\infty^p \tag{40b}$$

$$\Delta T^m = \xi^2 \frac{\widehat{D}_{xx}^m}{\widehat{D}_{xx}^p} \frac{\widehat{N}_{Tx}^p}{\widehat{N}_{Tx}^m} \Delta T^p \tag{40c}$$

The scaling factor for time is determined using Eq. (39b),

$$\Delta t^m = \frac{1}{\xi^2}\sqrt{\frac{\widehat{D}_{xx}^p}{\widehat{D}_{xx}^m}\frac{\hat{I}^m}{\hat{I}^p}}\Delta t^p \tag{41}$$

### *6.1.3 Numerical Scaling by Optimization*

The numerical scaling laws of the aeroelastic problem are generated by finding the scaled models for different geometric scales. For each geometric scale, the model configuration is found by solving an SO problem. The objective is the difference between the nondimensional structural responses of the prototype and the model, as in Eq. (17a),

$$J_u(\mathbf{d}; \{\mathbf{u}_i^m\}) = \sqrt{\sum_{i=1}^{100} \left\| \frac{\mathbf{u}_i^m}{\hat{u}^m} - \frac{\mathbf{u}_i^p}{\hat{u}^p} \right\|^2} \tag{42}$$

Note that in Eq. (42), the objective is computed based on the first 100 time steps of simulation, which corresponds to the first oscillation period of the aeroelastic response. The number of time steps is sufficiently large, so that the numerical result captures the characteristics of the aeroelastic responses associated with different model configurations. The number of time steps is also sufficiently small, so as to reduce the computational cost of sample generation in the BO algorithm.

An aeroelastically scaled model should result in a difference of zero, $J_u = 0$. The time step size for the aeroelastic simulation of the model is determined using Eq. (41). The time step size is the only quantity in the numerical scaling approach that is determined using an analytical similarity parameter.

The design variables include the thickness $h$, freestream pressure $p_\infty$, and temperature increment $\Delta T$ associated with the model. The constraints of the design variables are summarized in Table 3.

The SO problem is solved using the BO algorithm. The optimizer employs the LCB acquisition function with $\upsilon = 1.0$. The optimization is initialized with 10 samples and run for 300 iterations. In the inner optimization loop, the acquisition function is minimized using a gradient-based solver with multiple starts.

Table 3: Constraints of the design variables for the aeroelastically scaled model

| Design variables | $h$ (mm) | $p_\infty$ (kPa) | $\Delta T$ (K) |
|---|---|---|---|
| Range | $[0.2, 1.2]$ | $[3.0, 11.0]$ | $[0.5, 4.5]$ |

### *6.1.4 Numerical Scaling Results*

The scaled models are generated for three different geometric scales, $\xi = 2, 3, 4$. In each case, the convergence history is illustrated in Fig. 13, and the optimizer successfully converges within 300 iterations.

The nondimensional aeroelastic responses of the prototype and the models are compared in Fig. 14. In the first 100 time steps, the responses are used for the numerical scaling with the objective Eq. (42), and the responses of the scaled models match very well with the prototype response with errors less than 4%. For the responses beyond the first 100 time steps, the model and prototype responses still match reasonably well, especially the frequency and amplitude of the oscillation. The similarity parameters associated with the prototype and the scaled models are almost identical, as shown in Table 4. Finally, the scaling of the design variables are compared in Fig. 15. It is clear that the two-pronged approach has successfully generated the numerical scaling laws that *recover* the analytical scaling laws for the aeroelastic problem considered in this section.

Finally, the results also show that the BO algorithm is effective in finding the global minimum of the non-convex optimization problem associated with the two-pronged approach. As an example, the contour of $J_u$ w.r.t. variables $p_\infty$ and $\Delta T$ for the case $\xi = 4$ is illustrated in Fig. 16. The distribution of the objective $J_u$ is highly non-convex. While the global minimum of $J_u$ is achieved at the point that corresponds to an aeroelastically scaled model, there are multiple local minima that can lead to incorrectly scaled models. Nevertheless, the BO algorithm is able to avoid the local minima and identify the global minimum successfully.

Table 4: Optimization results for different geometric scales

| Parameters | $\frac{\hat{h}}{\hat{L}}$ | $\bar{\lambda}_F$ | $\frac{\Delta T \widehat{N}_{Tx} \hat{L}^2}{\widehat{D}_{xx}}$ |
|---|---|---|---|
| Prototype | 0.002 | 566.07 | 47.882 |
| $\xi = 2$ | 0.00201 (0.379%) | 566.85 (0.137%) | 47.581 (0.629%) |
| $\xi = 3$ | 0.00200 (0.167%) | 561.38 (0.829%) | 47.759 (0.257%) |
| $\xi = 4$ | 0.00200 (0.166%) | 566.69 (0.109%) | 47.671 (0.439%) |

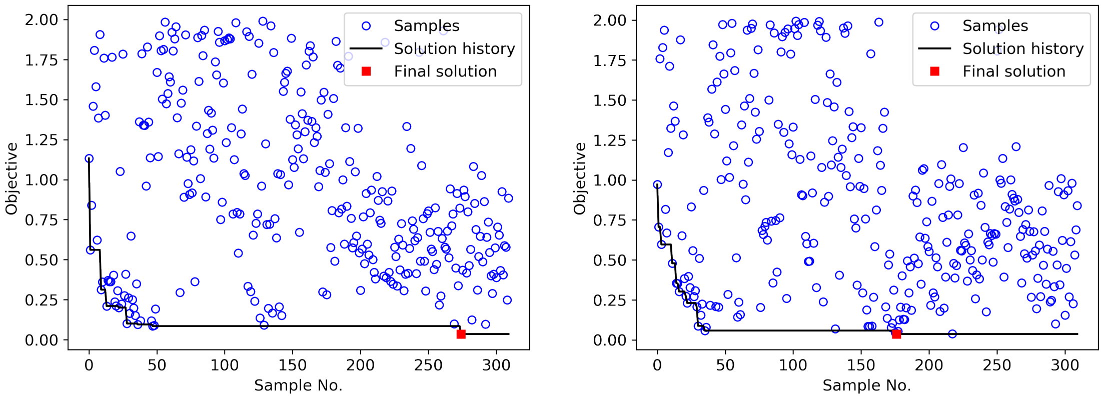

**(a)** $\xi = 2$ **(b)** $\xi = 3$

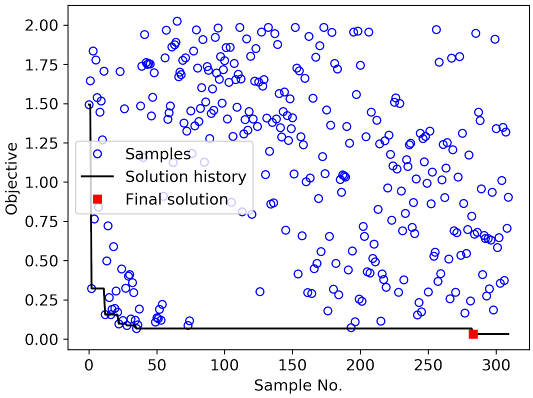

**(c)** $\xi = 4$

Figure 13: Convergence history of the cases for $\xi = 2, 3, 4$

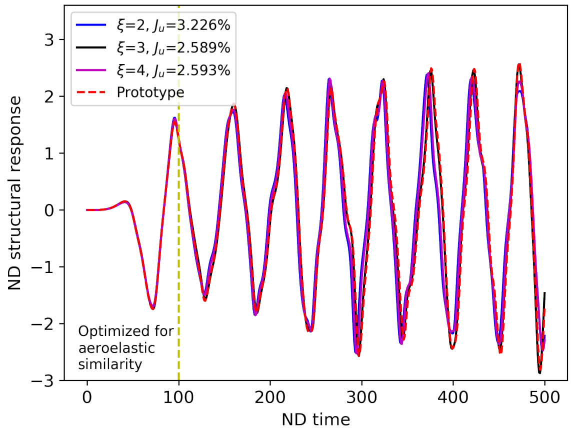

Figure 14: Nondimensional aeroelastic responses of the prototype and the scaled models

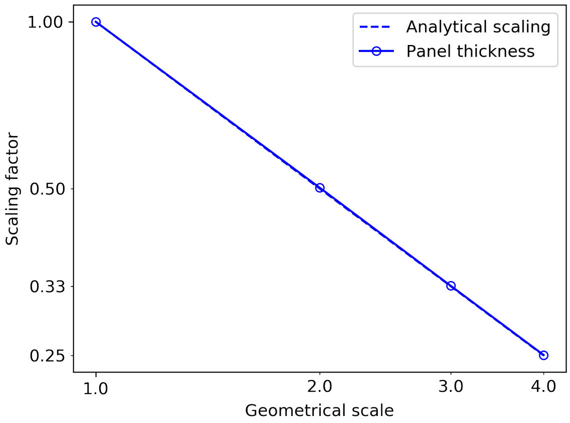

Figure 15: Comparison of analytical and numerical scaling

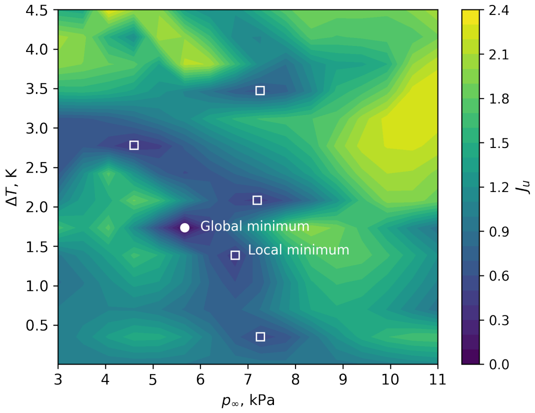

Figure 16: Contour of $J_u$ at $h = 0.5$mm for the case $\xi = 4$

## 6.2 Scaling of Quasi-Steady Aerothermoelastic Response

### 6.2.1 *Problem Description*

The "prototype" configuration is illustrated in Fig. 12. The case consists of a simply-supported square panel with side length of 1m and front rigid wall length of 1m. The flow is aligned with the panel, i.e. the flow orientation angle is zero. The layup of the panel is shown in Table 5, which resembles the honeycomb sandwich panel used in Ref. [3]. It is assumed that (1) honeycomb cell is hexagonal, so the material properties of the honeycomb core are isotropic in the $x$ and $y$ directions; (2) the honeycomb core carries only the shear stress and transfers the load between the upper and lower surfaces through shear deformation. The effective transverse shear modulus is computed using the analytical relation provided in Ref. [68]. The thermal properties of the honeycomb is obtained using the Swann-Pittman relation [69]. The effective thermal conductivity increases with temperature due to the radiative heat transfer. The emissivity of the upper surface is assumed to be 0.85. The "model" panel is a square *isotropic* panel made of Ti 6242. The material properties of both the prototype and the model are temperature dependent and the properties at room temperature ($T = 300K$) have been provided in Table 2.

The objective of the scaling is to determine the geometrical dimensions of the model panel, as well as the experimental conditions of the wind tunnel, so that the aerothermoelastic response of the model in the wind tunnel is similar to the aerothermoelastic response of the prototype at a given flight condition. The error of the structural response $J_u$ is quantified by the difference in the deflection at the center of the panel nondimensionalized by the thickness. The error of the thermal response $J_T$ is quantified by the difference in the average body temperature nondimensionalized by the stagnation temperature. The duration of the response of the prototype is 160s and the initial temperature of the prototype is 300K.

The fluid ROM for the prototype panel configuration has been developed in Ref. [21], and it is employed in the numerical aerothermoelastic simulation of the prototype and the model. The ROM was generated for flight conditions $M_\infty = 6.0$ and $H = 25$km. When combined with the correction and scaling technique, the ROM can be used to predict the aerodynamic loading and heating at different conditions for a flight envelope covering the range of $5.0 \leq M_\infty \leq 7.0$ and $20 \leq H \leq 30$km on the prototype as well as the model with a geometric scale $2 \leq \xi \leq 5$.

Table 5: Layup of the prototype panel

| Component | Material | Thickness |
|---|---|---|
| Upper sheet | Inconel 718 | 1 mm |
| Honeycomb core | Inconel 718 | 16 mm |
| Lower sheet | Inconel 718 | 1 mm |

Several wind tunnels that are suitable for hypersonic aerothermoelastic testing are illustrated in Fig. 3. Among these wind tunnels, the Hypersonic Tunnel Facility (HTF) at NASA Glenn Research Center is of interest [15, 17]. The HTF is a free-jet blow-down wind tunnel that is capable of simulating the flight conditions at multiple Mach numbers, $M_\infty = 5, 6, 7$, which are representative of the flight envelope of interest, as illustrated in Fig. 17. The test conditions at different Mach numbers are achieved using three nozzle configurations, all of which have an exit diameter of $42\text{in} \approx 1.07\text{m}$. The dimensions of the test section are $42\text{in} \times 10\text{ft} \approx 1.07\text{m} \times 3.05\text{m}$.

The constraints representing the operating envelope of the HTF are necessary for the optimization problem associated with refined aerothermoelastic scaling. However, the data defining the *exact* operating envelope of the HTF is unavailable in the open literature. The only public data available is the upper and lower limits of the stagnation temperature and pressure of the operating envelope at $M_\infty = 5, 6, 7$ [15, 17]. Therefore, in the current study, three sets of “realistic” wind tunnel conditions are synthesized based on the available HTF data in public [15, 17], illustrated in Fig. 18 and listed in Table 6. Additionally, a set of “ideal” wind tunnel conditions is assumed based on the flight condition of $5 \leq M_\infty \leq 7$ and $20\text{km} \leq H \leq 30\text{km}$, which encompasses the ranges of the three sets of “realistic” wind tunnel conditions. For each set of the conditions, the Mach number is fixed and it is assumed that an arbitrary combination of the stagnation temperature and pressure in the given range is attainable.

Another constraining factor for the aerothermoelastic test is the operation time of the wind tunnel. In the quasi-steady aerothermoelastic problem, the scaling in time is determined by the Fourier number, as required by Eq. (16a),

$$t^m = \frac{1}{\xi^2} \frac{[\hat{k}^s]^p}{[\hat{\rho}^s \hat{c}_p^s]^p} \frac{[\hat{\rho}^s \hat{c}_p^s]^m}{[\hat{k}^s]^m} t^p \tag{43}$$

It means that the time duration of the the scaled test is inversely proportional to the square of the geometric scale $\xi$. When the time duration of the quasi-steady aerothermoelastic response is 160s, and the geometric scale ranges from 2 to 5, the time duration of the the scaled test is expected to be less than 40s. The operation time of the HTF depends on the test condition and ranges from 42s to 294s. Therefore, it is assumed that the wind tunnel can operate for sufficient time length so as to accommodate the aerothermoelastic test of any model with geometric scales of $2 \leq \xi \leq 5$. In other words, no constraint is needed for the time duration of the scaled test in the optimization problem associated with refined aerothermoelastic scaling.

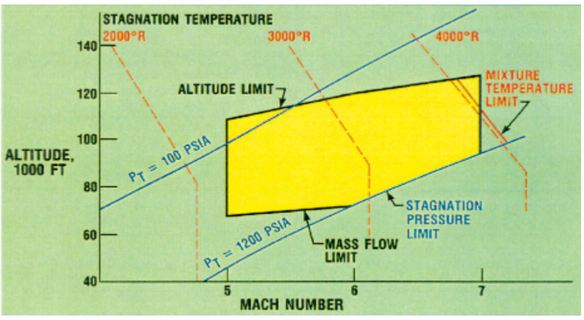

Figure 17: Operating envelope of the HTF (Figure 1 of Ref. [15])

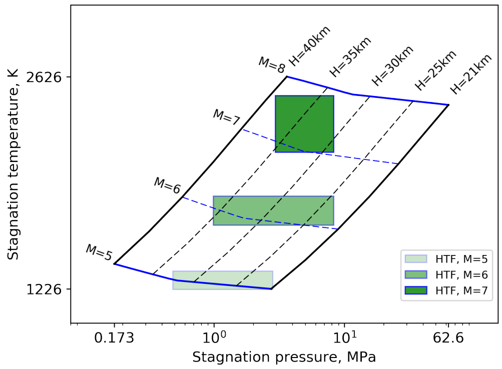

Figure 18: Envelopes of the HTF test conditions and typical hypersonic flight conditions

Table 6: Wind tunnel conditions

| | | $M_\infty$ | $p_0$ (MPa) | $T_0$ (K) |
|---|---|---|---|---|
| Ideal | | $[5, 7]$ | $[0.27579, 86.184466]$ | $[416.483, 2500.0]$ |
| Realistic | WT5 | 5 | $[0.4860804, 2.82685]$ | $[1222.22, 1344.44]$ |
| | WT6 | 6 | $[0.992845, 8.273709]$ | $[1647.22, 1838.89]$ |
| | WT7 | 7 | $[2.96475, 8.273709]$ | $[2127.778, 2500.0]$ |

The design variables considered for the scaling of the skin panel, as well as their constraints, are summarized in Table 7. These design variables are selected from Table 1. The design variables consist of the wind tunnel conditions, geometrical parameters of the model, and the parameters for an external radiative heater. The constraints for the wind tunnel conditions have been provided in Table 6. In the constraints for the geometrical parameters, the upper limits are determined by the size of the wind tunnel test section and the lower limits are determined by the manufacturing constraints. The radiative heating is assumed to enable the discussion of the incomplete testing strategy. It is assumed that the radiation temperature $T_{rad}$ is constant throughout the test and the surface emissivity of the model $\varepsilon$ is uniformly distributed. The model is assumed to be aligned with the flow, so the inclination angle $\theta$ is zero. The model is built of a single material, Ti 6242, so the material properties are fixed and there is only one design variable $h$ representing the thickness of the panel.

When parameter relaxation strategy is employed, only the similarity parameters in Eqs. (16a) and (16c) are imposed as equality constraints, and the matching of the similarity parameters in

Table 7: Design variables for the scaled model and their constraints

| $M_\infty, p_0, T_0$ | $L$ (m) | $L_{le}$ (m) | $h$ (m) | $\varepsilon$ | $T_{rad}$ (K) |
|---|---|---|---|---|---|
| See Table 6 | $[0.1, 0.5]$ | $[0.1, 2.0]$ | $[0.001, 0.01]$ | $[0.5, 1.0]$ | $[300.0, 2500.0]$ |

Eq. (16b) is not required. Equation (16a) defines the scaling of the time step size during the simulation,

$$\Delta t^m = \frac{1}{\xi^2} \frac{[\hat{k}^s]^p}{[\hat{\rho}^s \hat{c}_p^s]^p} \frac{[\hat{\rho}^s \hat{c}_p^s]^m}{[\hat{k}^s]^m} \Delta t^p \tag{44}$$

Assuming $\hat{T}_T^p = \hat{T}_S^p = \hat{T}_w^p$ and $\hat{T}_F^p = T_\infty^p$ for the prototype, Eq. (16c) implies the following equality constraints on the design variables associated with reference temperatures,

$$\hat{T}_T^m = \hat{T}_S^m = \hat{T}_w^m, \quad \hat{T}_F^m = T_\infty^m, \quad \frac{T_w^m}{T_\infty^m} = \frac{T_w^p}{T_\infty^p} \tag{45}$$

### *6.2.2 Scaling With Ideal Wind Tunnel Conditions*

First, the feasibility of numerical aerothermoelastic scaling is explored by generating scaled models for different geometric scales with ideal wind tunnel conditions. The flight conditions of the prototype are $M_\infty = 6.0$ and $H = 25$km. The parameter relaxation strategy is used and the design variables include $M_\infty, p_0, T_0, L_{le}, h$. Four different geometric scales are considered: $\xi = 2, 3, 4, 5$. For each case, 20 samples are generated to initialize the SBO algorithm and 50 iterations are conducted during the optimization.

The Pareto fronts for the four cases are shown in Fig. 19. The results show that, reducing the error of one of responses would result in a rapid increase in the error of the other response. Thus it illustrates the failure of the classical aerothermoelastic scaling. Nevertheless, for each geometric scale, it is possible to find a model configuration that satisfies approximately the aerothermoelastic similarity, as indicated by the solid points in Fig. 19. These points are assumed to be the final design points. The responses associated with these design points are shown in Figs. 20 and 21. In all the cases, the errors in the aerothermoelastic responses are less than 10%.

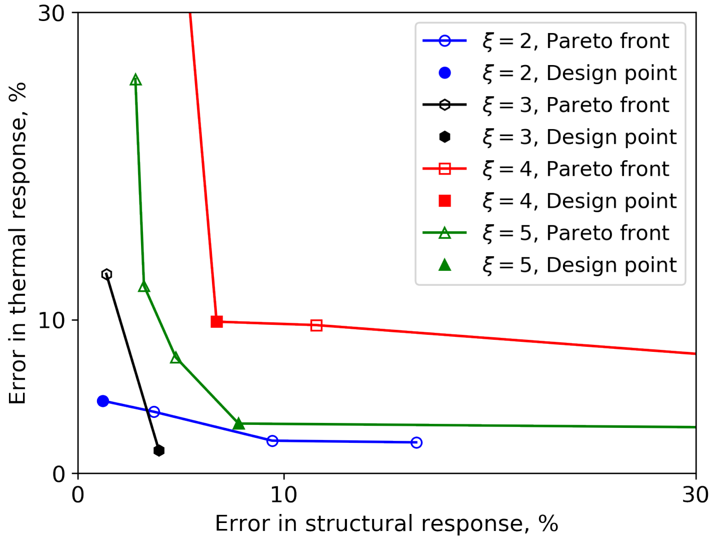

Figure 19: Pareto fronts for different geometric scales

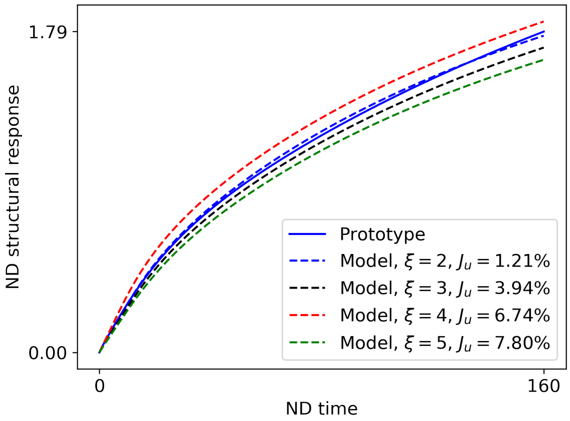

Figure 20: Comparison of nondimensional structural responses

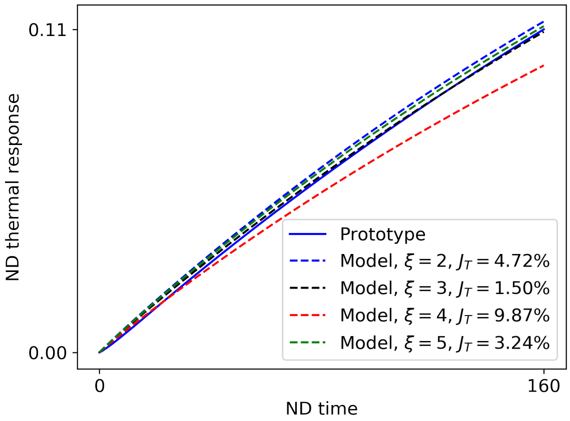

Figure 21: Comparison of nondimensional thermal responses

The values of the design variables are listed in Table 8 and illustrated in Fig. 22. Figure 22 illustrates the differing scaling requirements of the geometrical variables $h$ and $L_{le}$. The numerical scaling of the panel thickness $h$ agrees with the analytical scaling requirements represented by the blue dashed line. However, the variable $L_{le}$ increases as the panel dimension decreases, which is vastly different from the analytical scaling requirements. The scaling of $L_{le}$ obtained numerically represents a refinement of the analytical scaling relation. Table 8 illustrates the activation of constraints at the design points. The constraints of $h$ and $L_{le}$ are active for the cases $\xi = 2$ and $\xi = 3$, respectively, due to the limitation in the size of the test section. Using the classical scaling approach, it is inconvenient to develop a scaled model that accounts for the inequality constraints. That is because, for the classical approach the scaling requirements are determined by the analytical similarity parameters. However, the derivation of these similarity parameters does not involve any inequality constraints. Nevertheless, the inequality constraints are treated efficiently using the two-pronged approach. A scaled model that satisfies all the constraints is obtained by the refined and systematic adjustment using the optimization process of the two-pronged approach.

To summarize, the results in this section show that it is possible to achieve refined ASL under ideal wind tunnel conditions using the two-pronged approach. Furthermore, the results obtained illustrate the advantages of the two-pronged approach over the classical scaling approach. First, the two-pronged approach can generate the requirements for aerothermoelastic scaling by refining the scaling requirements represented by the analytical similarity parameters. Second, the two-pronged approach can account for the inequality constraints representing the limitations of the wind tunnel and manufacturing capabilities, which cannot be treated efficiently using the classical approach.

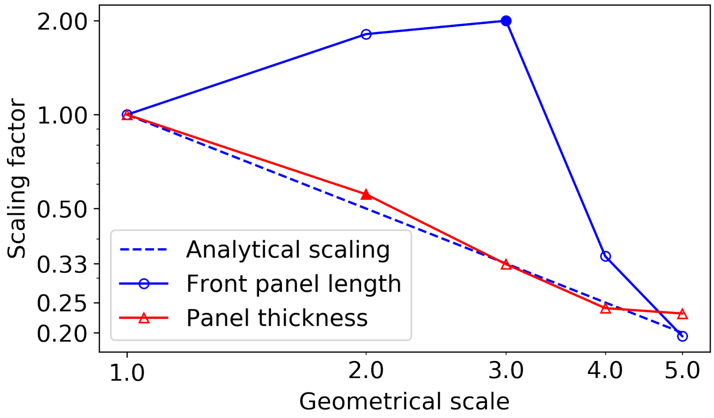

Figure 22: Analytical and numerical scaling of geometrical variables

Table 8: Design points for different geometric scales

| Design variables | $\xi = 2$ | $\xi = 3$ | $\xi = 4$ | $\xi = 5$ |
|---|---|---|---|---|
| $M_\infty$ | 6.841e+00 | 5.653e+00 | 5.407e+00 | 6.250e+00 |
| $p_0$ (MPa) | 6.476e+01 | 3.916e+01 | 3.858e+01 | 7.330e+01 |
| $T_0$ (K) | 2.280e+03 | 1.868e+03 | 2.130e+03 | 2.187e+03 |
| $L_{le}$ (m) | 1.812e+00 | 2.000e+00 | 3.516e-01 | 1.950e-01 |
| $h$ (m) | 1.000e-02 | 5.971e-03 | 4.317e-03 | 4.150e-03 |

### *6.2.3 Scaling With Realistic Wind Tunnel Conditions*

Next, the scaling of the prototype is conducted with realistic wind tunnel conditions. The flight conditions of the prototype are $M_\infty = 6.0$ and $H = 25$km and the wind tunnel conditions WT5, WT6 and WT7 from Table 6 are used. Two cases are considered. For Case 1, pure parameter relaxation strategy is used and the design variables are $p_0, T_0, L, L_{le}, h$. For Case 2, combined strategy of parameter relaxation and incomplete testing is used and the design variables are $p_0, T_0, L, L_{le}, h, \varepsilon, T_{rad}$. For both cases, 20 samples are generated to initialize the SBO algorithm and 50 iterations are conducted for the optimization.

The Pareto fronts of the two cases are shown in Fig. 23. For Case 1, the two-pronged approach failed to find any good solution that have low errors in the structural and thermal responses for any realistic wind tunnel conditions. For Case 2, it is possible to find configurations that can satisfy approximately the aerothermoelastic similarity for all the three wind tunnel conditions. The differences between the two cases are explained by examining the design points in Tables 9-10. All the design points in Case 1 have reached the upper limit of $p_0$ for the realistic wind tunnel conditions, which is less than 10% of the maximum $p_0$ in the ideal wind tunnel conditions. As illustrated in Fig. 24, the low value of $p_0$ leads to insufficient heating on the model and produces a slow increase in the average temperature as well as the center deflection. The problem in Case 1 is resolved in Case 2 with the introduction of the external heating, which compensates for the low heating rate in the realistic wind tunnel conditions.

Table 9: Design points for realistic wind tunnel conditions in Case 1

| Design variables | WT5 | WT6 | WT7 |
|---|---|---|---|
| $p_0$ (MPa) | 2.827e+00 | 8.274e+00 | 8.274e+00 |
| $T_0$ (K) | 1.267e+03 | 1.664e+03 | 2.317e+03 |
| $L$ (m) | 5.000e-01 | 5.000e-01 | 5.000e-01 |
| $L_{le}$ (m) | 7.601e-01 | 6.270e-01 | 6.419e-01 |
| $h$ (m) | 7.034e-03 | 8.794e-03 | 1.000e-02 |

Table 10: Design points for realistic wind tunnel conditions in Case 2

| Design variables | WT5 | WT6 | WT7 |
|---|---|---|---|
| $p_0$ (MPa) | 4.861e-01 | 9.928e-01 | 6.543e+00 |
| $T_0$ (K) | 1.222e+03 | 1.821e+03 | 2.220e+03 |
| $L$ (m) | 5.000e-01 | 4.480e-01 | 4.448e-01 |
| $L_{le}$ (m) | 2.000e+00 | 1.761e+00 | 1.717e+00 |
| $h$ (m) | 7.500e-03 | 7.798e-03 | 8.210e-03 |
| $\varepsilon$ | 5.000e-01 | 1.000e+00 | 1.000e+00 |
| $T_{rad}$ (K) | 1.621e+03 | 1.492e+03 | 1.548e+03 |

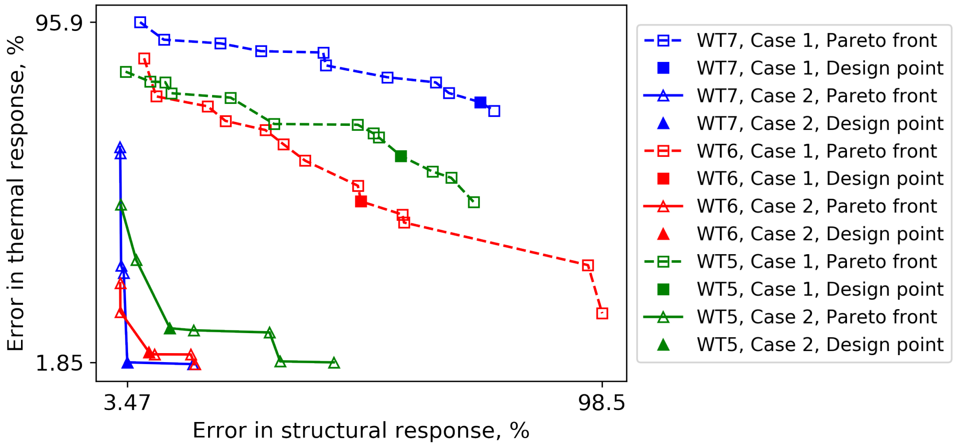

Figure 23: Pareto fronts for Cases 1 and 2

The comparison between Cases 1 and 2 shows that, using parameter relaxation and incomplete testing, the two-pronged approach can be used to generate aerothermoelastically scaled models with restrictive constraints of realistic wind tunnel conditions. However, it should be emphasized that achieving small errors in the structural and thermal responses is progressively more difficult as the Mach number decreases. When $M_\infty = 5$, the design point has most of the constraints active, indicating that the constraints imposed by the wind tunnel conditions WT5 are not suitable for the flight condition considered in the current problem.

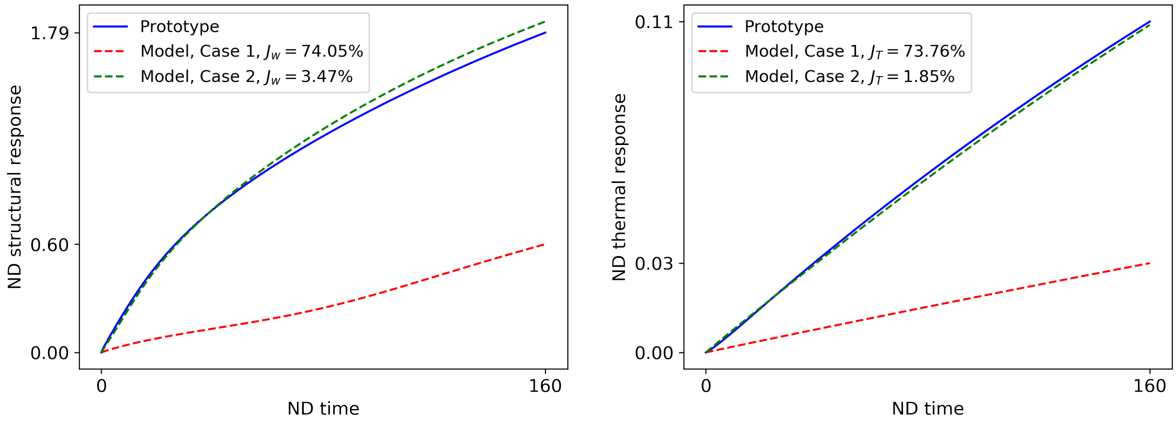

**(a) Nondimensional structural response** **(b) Nondimensional thermal response**

Figure 24: Comparison of prototype and model responses in Cases 1 and 2 for wind tunnel condition WT7.

#### *6.2.4 Scaling for Multiple Flight Conditions in the Same Wind Tunnel*

Finally, the two-pronged approach is used to generate scaled models for aerothermoelastic testing associated with different flight conditions using the same set of wind tunnel conditions. A range of flight conditions is considered: $M_\infty = 5.0, 5.5, 6.0, 6.5, 7.0$ and $H = 20, 22, 25, 28, 30$km. The wind tunnel condition WT7 in Table 6 is assumed. The design variables are $p_0, T_0, L, L_{le}, h, \varepsilon, T_{rad}$, which are the same as those in the previous problem. However, in this problem, instead of solving the MO problem for each flight condition, an SO problem is solved for a combined objective function,

$$J_s = \sqrt{J_u^2 + J_T^2} \tag{46}$$

Solving SO problems requires fewer samples of numerical aerothermoelastic responses and thus saves a considerable amount of computer time. The SO problems are solved in a sequential manner. The first SO problem is initialized using 20 samples and 20 iterations are conducted. Next, the SO problems are solved using 20 iterations with the initial samples recycled from the previous SO problems.

The errors associated with different flight conditions are listed in Table 11. For all but five flight conditions, it is possible to find configurations that can approximately satisfy the aerothermoelastic similarity with errors of less than 5%. The errors exceed 5% in two cases: (1) high Mach number ($M_\infty = 6.5, 7.0$) and low altitude ($H = 20$km) and (2) low Mach number ($M_\infty = 5.0, 5.5$) and high altitude ($H = 28, 30$km).

Next, three typical cases are examined: (1) $M_\infty = 7.0, H = 20$km, ($J_s = 5.22\%$), (2) $M_\infty = 6.0, H = 22$km, ($J_s = 1.50\%$), (3) $M_\infty = 5.0, H = 30$km, ($J_s = 9.98\%$). Figure 25 illustrates the structural deformation and temperature distribution along the centerline at nondimensional times $t = 30, 90, 160$. For all the cases, aerothermoelastic similarity is achieved approximately. However, the temperature distribution of the prototype is more non-uniform than the model, because the heat sources on the model include both aerodynamic heating and external heating due to radiation. While the aerodynamic heating is stronger near the leading edge of the panel, the radiative heating is almost uniform over the panel. This produces a relatively uniform temperature distribution on the model. The temperature distribution becomes more non-uniform as the Mach number increases and the altitude decreases, because the aerodynamic heating becomes stronger at higher Mach number and higher freestream pressure, i.e.

lower altitude. In the long-term quasi-steady aerothermoelastic response, the panel deformation is mainly caused by the thermal effect [31]. The maximum deflection of the panel increases as the average temperature increases and the location of the maximum deflection of the panel is closer to the leading edge when the temperature distribution is more non-uniform.

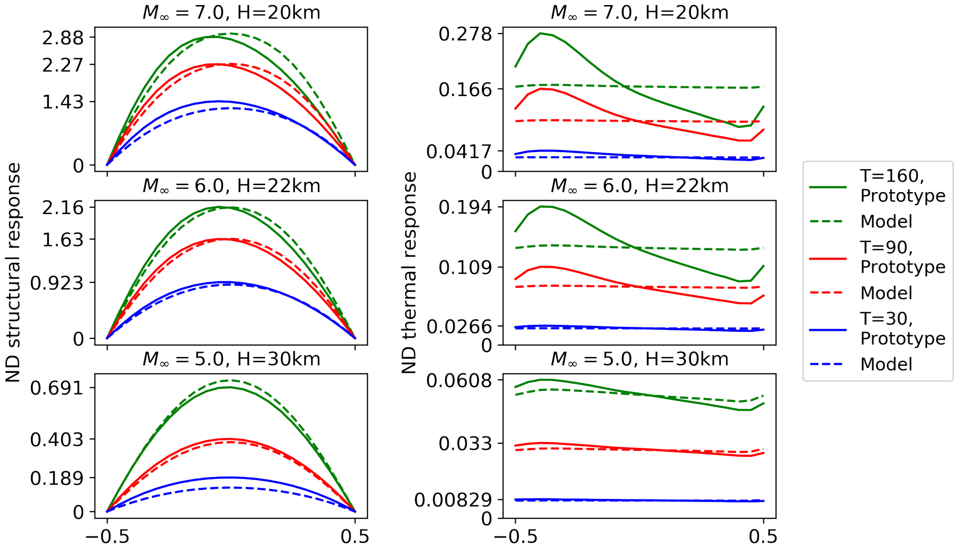

Figure 25: Nondimensional structural and thermal responses of selected cases

Among the three sets of flight conditions considered, the second one is a typical case where aerothermoelastic similarity is achieved approximately. The temperature distribution of the prototype is not highly non-uniform, so that the maximum deflections of the prototype and the model occur approximately at the center of the panel. The average temperatures of the prototype and the model are similar, resulting in similar amplitudes of structural deformation and smaller errors in the structural response. On the other hand, the first set of flight conditions represents a case where the aerodynamic heating is too strong and produces a highly non-uniform temperature distribution that causes the location of maximum deflection of the prototype to move from the center towards the leading edge. The mismatch in the shape of panel deflection produces an increased error in the nondimensional structural response. The third set of flight conditions represents the case where the aerodynamic heating is weak but the external heating is insufficient to accurately control the average temperature of the model. The mismatch in the average temperatures of the model and the prototype leads to the error in the magnitude of panel deflection and the increased error of structural response.

Within the current optimization framework, the sources of errors in the first and the third cases can be minimized or eliminated by refined adjustment of the model. For the first case, the *distribution* of the radiation temperature of the radiative heater can be optimized, so as to tune the distribution of the radiative heat flux to resemble the non-uniform distribution of the aerodynamic heat flux. Furthermore, the objective functions $J_u$ and $J_T$ can be modified to include the structural and thermal modal coordinates so as to ensure the matching of the distributions of deformation and temperature. For the third case, the time variation of the radiation temperature during the wind tunnel test can be optimized, so as to accurately control the average temperature and thus the deformation of the panel.

Table 11: Errors in aerothermoelastic responses of differernt flight conditions (in %)

| | $H = 20\text{km}$ | $H = 22\text{km}$ | $H = 25\text{km}$ | $H = 28\text{km}$ | $H = 30\text{km}$ |
|---|---|---|---|---|---|
| $M_\infty = 5.0$ | 4.82 | 4.41 | 3.69 | 7.20 | 9.98 |
| $M_\infty = 5.5$ | 3.40 | 2.95 | 3.34 | 4.51 | 5.47 |
| $M_\infty = 6.0$ | 2.75 | 1.50 | 4.52 | 3.2 | 4.13 |
| $M_\infty = 6.5$ | 6.16 | 2.15 | 3.24 | 2.25 | 2.81 |
| $M_\infty = 7.0$ | 5.22 | 3.58 | 2.43 | 5.17 | 2.01 |

## 7 CONCLUSIONS

This study examines the problem of hypersonic aerothermoelastic scaling employing a novel two-pronged approach. It combines the classical scaling approach with augmentation from numerical simulations of the specific problem based on a constrained optimization formulation. In the optimization formulation, the strategies of parameter relaxation and incomplete testing are incorporated to assist the refinement of hypersonic aerothermoelastic scaling. The new two-pronged approach was applied to the aerothermoelastic scaling of a skin panel in hypersonic flow. The aerothermoelastic similarity between the prototype and the scaled model was successfully obtained using a systematic optimization approach, which accounts for realistic constraints of the wind tunnel and manufacturing.

The principal conclusions are summarized below,

1. When the wind tunnel is capable of simulating flight conditions with sufficiently high stagnation temperature and stagnation pressure, the aerothermoelastic scaling can be achieved using a parameter relaxation strategy. An aerothermoelastically scaled model is constructed by matching a partial set of the aerothermoelastic similarity parameters between the prototype and the model.
2. When the wind tunnel is limited and cannot provide high stagnation temperature or stagnation pressure, aerothermoelastic similarity can be still achieved by combining parameter relaxation with incomplete testing. Thus external loading and heating is introduced to compensate for the insufficient aerodynamic loading and heating capability of the wind tunnel.
3. Using one set of wind tunnel conditions, i.e. in the same wind tunnel, it is possible to adjust the scaled model in a refined manner, so as to conduct hypersonic aerothermoelastic testing for a range of flight conditions that are representative of the flight envelope of a hypersonic vehicle.

The aerothermoelastic scaling approach described in this study can be applied to testing components of a hypersonic vehicle. Furthermore, the approach can be used to map aerothermoelastic results obtained in wind tunnel tests on scaled vehicles to a full-scale vehicle. Therefore, it has the potential for saving considerable funds in the development process of future hypersonic vehicles.

## 8 REFERENCES

[1] George Tzong, Richard Jacobs, and Salvatore Liguore (2010). Predictive Capability for Hypersonic Structural Response and Life Prediction, Phase 1 – Identification of Knowledge Gaps, Volume I. Tech. Rep. AFRL-RB-WP-TR-2010-3068,V1, Wright-Patterson Air Force Base, Dayton, OH.

[2] McNamara, J. J. and Friedmann, P. P. (2011). Aeroelastic and Aerothermoelastic Analysis in Hypersonic Flow: Past, Present, and Future. *AIAA Journal*, 49(6), 1089–1122. doi: 10.2514/1.J050882.

[3] Zuchowski, B. (2012). Predictive capability for hypersonic structural response and life prediction: Phase ii – detailed design of hypersonic cruise vehicle hot-structure. Tech. Rep. AFRL-RQ-WP-TR-2012-0280, Wright-Patterson Air Force Base, Dayton, OH.

[4] Bowcutt, K. G. (2018). Physics drivers of hypersonic vehicle design. In *AIAA 2018–5373, 22nd AIAA International Space Planes and Hypersonics Systems and Technologies Conference*. Orlando, FL, pp. 1–22. doi:10.2514/6.2018-5373.

[5] Calligeros, J. M. and Dugundji, J. (1959). Similarity Laws Required for Experimental Aerothermoelastic Studies. Tech. Rep. TR 75–1, Office of Naval Research.

[6] Calligeros, J. M. and Dugundji, J. (1961). Similarity Laws Required for Experimental Aerothermoelastic Studies. Part 2 Hypersonic Speeds. Tech. Rep. TR 75–2, Office of Naval Research.

[7] Dugundji, J. and Calligeros, J. M. (1962). Similarity laws for aerothermoelastic testing. *Journal of the Aerospace Sciences*, 29(8), 935–950. doi:10.2514/8.9663.

[8] McClinton, C. R. (2006). X-43 Scramjet Power Breaks the Hypersonic Barrier: Dryden Lectureship in Research for 2006. In *AIAA 20061, Proceedings of 44th AIAA Aerospace Sciences Meeting and Exhibit*. Reno, Nevada, pp. 1–18. doi:10.2514/6.2006-1.

[9] Hank, J., Murphy, J., and Mutzman, R. (2008). The X-51A scramjet engine flight demonstration program. In *AIAA 2008–2540, 15th AIAA International Space Planes and Hypersonic Systems and Technologies Conference*. Dayton, OH, pp. 1–13. doi: 10.2514/6.2008-2540.

[10] Lockheed-Martin (2013). Meet the SR-72. `http://www.lockheedmartin.com/us/news/features/2013/sr-72.html`. Accessed: 03/27/2019.

[11] Boeing (2018). Early look: This aircraft concept shows a hypersonic vehicle for passengers. `https://www.boeing.com/features/2018/06/hypersonic-concept-vehicle.page`. Accessed: 11/16/2018.

[12] Lamorte, N., Friedmann, P. P., Dalle, D. J., et al. (2014). Uncertainty propagation in integrated airframe–propulsion system analysis for hypersonic vehicles. *Journal of Propulsion and Power*, 31(1), 54–68.

[13] Lu, F. K. and Marren, D. E. (2002). *Advanced Hypersonic Test Facilities*, Vol. 198, Chap. 10. AIAA, pp. 279–314.

[14] Witeof, Z. (2013). *Exploratory Study on the Design of Combined Aero-Thermo-Structural Experiments in High Speed Flows*. PhD Thesis, The Ohio State University, Columbus, OH.

[15] Woike, M. and Willis, B. (2000). Mach 6 integrated systems testing for the hypersonic tunnel facility. In *AIAA 2000–2446, 21st Aerodynamic Measurement Technology and Ground Testing Conference*. Denver, CO, pp. 1–10. doi:10.2514/6.2000-2446.

[16] David, K., Gorham, J., Kim, S., et al. (2006). Aeronautical Wind Tunnels, Europe and Asia. Tech. rep., Federal Research Division Library of Congress, Washington, DC.

[17] Goodrich, M. and Gorham, J. (2008). Wind Tunnels of the Western Hemisphere. Tech. rep., Federal Research Division Library of Congress, Washington, DC.

[18] Riley, Z. B., Perez, R. A., Bartram, G. W., et al. (2019). Aerothermoelastic experimental design for the AEDC/VKF tunnel C: Challenges associated with measuring the response of flexible panels in high-temperature, high-speed wind tunnels. *Journal of Sound and Vibration*, 441, 96–105. doi:10.1016/j.jsv.2018.10.022.

[19] Huang, D., Rokita, T., and Friedmann, P. P. (2017). Efficient Reduced-Order Modeling for Skin Panels in Hypersonic Flow and Its Application to Generating Aerothermoelastic Scaling Laws. In *International Forum on Aeroelasticity and Structural Dynamics*. Como, Italy, pp. 1–29.

[20] Huang, D., Rokita, T., and Friedmann, P. P. (2018). Aerothermoelastic Scaling Laws for Hypersonic Skin Panel Configurations with Arbitrary Flow Orientation. In *AIAA Paper 2018–1684, 2018 AIAA/ASCE/AHS/ASC Structures, Structural Dynamics, and Materials Conference*. Kissimmee, FL, pp. 1–23. doi:10.2514/6.2018-1684.

[21] Huang, D., Friedmann, P. P., and Rokita, T. ((Accepted)). Aerothermoelastic scaling laws for hypersonic skin panel configurations with arbitrary flow orientation. *AIAA Journal*.

[22] Friedmann, P. (2004). Aeroelastic scaling for rotary-wing aircraft with applications. *Journal of Fluids and Structures*, 19(5), 635–650. doi:10.1016/j.jfluidstructs.2004.03.003.

[23] Kaviany, M. (2002). *Principles of Heat Transfer*, Chap. 1. John Wiley & Sons, pp. 24–32.

[24] Culler, A. J. and McNamara, J. J. (2011). Impact of Fluid-Thermal-Structural Coupling on Response Prediction of Hypersonic Skin Panels. *AIAA Journal*, 49(11), 2393–2406. doi:10.2514/1.J050617.

[25] Thornton, E. A. (1996). *Thermal Structures for Aerospace Applications*. Reston, VA: American Institute of Aeronautics and Astronautics.

[26] Reddy, J. N. (2004). *Mechanics of Laminated Composite Plates and Shells: Theory and Analysis*. New York: CRC Press.

[27] Anderson, J. D. (2006). *Hypersonic and High Temperature Gas Dynamics*. AIAA.

[28] Tsien, H.-S. (1946). Similarity Laws of Hypersonic Flows. *Studies in Applied Mathematics*, 25(1–4), 247–251.

[29] Hayes, W. D. and Probstein, R. F. (1959). Viscous Hypersonic Similitude. *Journal of the Aerospace Sciences*, 26(12), 815–824.

[30] Huang, D., Rokita, T., and Friedmann, P. P. (2017). An aerothermoelastic analysis framework enhanced by model order reduction with applications. In *AIAA 2017–1601, 58th AIAA/ASCE/AHS/ASC Structures, Structural Dynamics, and Materials Conference*. Grapevine, TX, pp. 1–19. doi:10.2514/6.2017-1601.

[31] Huang, D., Rokita, T., and Friedmann, P. P. (2018). An integrated aerothermoelastic analysis framework with application to skin panels. *AIAA Journal*. doi:10.2514/1.J056677.

[32] Hodges, D. H. and Pierce, G. A. (2011). *Introduction to Structural Dynamics and Aeroelasticity*, Vol. 15, Chap. 5. Cambridge University Press, pp. 175–200. doi: 10.1017/CBO9780511997112.

[33] Ashley, H. and Zartarian, G. (1956). Piston theory – a new aerodynamic tool for the aeroelastician. *Journal of the Aeronautical Sciences*, 23(12), 1109–1118. doi:10.2514/8.3740.

[34] Eckert, E. R. G. (1960). Survey of boundary layer heat transfer at high velocities and high temperatures. Tech. rep., Minnesota. Univ., Minneapolis. Heat Transfer Lab.

[35] van der Weide, E., Kalitzin, G., Schluter, J., et al. (2006). Unsteady Turbomachinery Computations Using Massively Parallel Platforms. In *AIAA Paper 2006–0421, 44th AIAA Aerospace Sciences Meeting and Exhibit*. Reno, NV, pp. 1–16. doi:10.2514/2006-0421.

[36] Kenway, G. K. W., Secco, N., Martins, J. R. R. A., et al. (2017). An efficient parallel overset method for aerodynamic shape optimization. In *AIAA 2017–0357, Proceedings of the 58th AIAA/ASCE/AHS/ASC Structures, Structural Dynamics, and Materials Conference, AIAA SciTech Formum*. Grapevine, TX, pp. 1–30. doi:10.2514/2017-0357.

[37] Crowell, A. R., McNamara, J., and Miller, B. (2011). Hypersonic aerothermoelastic response prediction of skin panels using computational fluid dynamic surrogates. *Journal of Aeroelasticity and Structural Dynamics*, 2(2). doi:10.3293/asdj.2011.11.

[38] Falkiewicz, N. J., S. Cesnik, C. E., Crowell, A. R., et al. (2011). Reduced-Order Aerothermoelastic Framework for Hypersonic Vehicle Control Simulation. *AIAA Journal*, 49(8), 1625–1646. doi:10.2514/1.J050802.

[39] Crowell, A. R. and McNamara, J. J. (2012). Model reduction of computational aerothermodynamics for hypersonic aerothermoelasticity. *AIAA Journal*, 50(1), 74–84. doi: 10.2514/1.J051094.

[40] Trussell, D. H. and Weidman, D. J. (1960). A radiant heater to simulate aerodynamic heating in a wind tunnel. Tech. Rep. NASA TN D–530, NASA Langley Research Center, Langley Field, VA.

[41] Forrester, A., Sobester, A., and Keane, A. (2008). *Engineering Design Via Surrogate Modelling: A Practical Guide*. John Wiley & Sons. doi:10.2514/4.479557.

[42] Bryan Glaz (2008). *Active/Passive Optimization of Helicopter Rotor Blades for Improved Vibration, Noise, and Performance Characteristics*. Ph.D. thesis, University of Michigan, Ann Arbor.

[43] Jones, D. R., Schonlau, M., and Welch, W. J. (1998). Efficient Global Optimization of Expensive Black-Box Functions. *Journal of Global Optimization*, 13(4), 455–492.

[44] Goel, T., Vaidyanathan, R., Haftka, R. T., et al. (2007). Response surface approximation of pareto optimal front in multi-objective optimization. *Computer Methods in Applied Mechanics and Engineering*, 196(4-6), 879–893. doi:10.1016/j.cma.2006.07.010.

[45] Sasena, M. J. (2002). *Flexibility and Efficiency Enhancements for Constrained Global Design Optimization with Kriging Approximations*. Ph.D. thesis, University of Michigan, Ann Arbor.

[46] Rasmussen, C. E. and Williams, C. K. I. (2006). *Gaussian Processes for Machine Learning*. Cambridge, MA: The MIT Press.

[47] Mockus, J. (1994). Application of Bayesian Approach to Numerical Methods of Global and Stochastic Optimization. *Journal of Global Optimization*, 4(4), 347–365.

[48] Martinez-Cantin, R. (2014). Bayesopt: A Bayesian Optimization Library for Nonlinear Optimization, Experimental Design and Bandits. *The Journal of Machine Learning Research*, 15(1), 3735–3739.

[49] Knowles, J. (2006). ParEGO: A Hybrid Algorithm With Online Landscape Approximation for Expensive Multiobjective Optimization Problems. *IEEE Transactions on Evolutionary Computation*, 10(1), 50–66. doi:10.1109/TEVC.2005.851274.

[50] Gelbart, M. A. (2015). *Constrained Bayesian Optimization and Applications*. Ph.D. thesis, Harvard University, Graduate School of Arts & Sciences, Cambridge, MA.

[51] Kushner, H. J. (1964). A New Method of Locating the Maximum Point of an Arbitrary Multipeak Curve in the Presence of Noise. *Journal of Basic Engineering*, 86(1), 97–106. doi:10.1115/1.3653121.

[52] Lizotte, D. J. (2008). *Practical Bayesian Optimization*. Ph.D. thesis, University of Alberta, Edmonton, Alta., Canada.

[53] Cox, D. D. and John, S. (1992). A Statistical Method for Global Optimization. In *Systems, Man and Cybernetics, 1992., IEEE International Conference on*. IEEE, pp. 1241–1246. doi:10.1109/ICSMC.1992.271617.

[54] Brochu, E., Cora, V. M., and De Freitas, N. (2010). A Tutorial on Bayesian Optimization of Expensive Cost Functions, with Application to Active User Modeling and Hierarchical Reinforcement Learning. *arXiv preprint arXiv:1012.2599*.

[55] Emmerich, M. and Klinkenberg, J.-w. (2008). The Computation of the Expected Improvement in Dominated Hypervolume of Pareto Front Approximations. Tech. Rep. LIACS-TR 9-2008, Rapport Technique, Leiden University, The Netherlands.

[56] Ponweiser, W., Wagner, T., Biermann, D., et al. (2008). Multiobjective Optimization on a Limited Budget of Evaluations Using Model-Assisted S-Metric Selection. In *International Conference on Parallel Problem Solving from Nature*, Vol. 5199. Berlin, Heidelberg: Springer, pp. 784–794. doi:10.1007/978-3-540-87700-4_78.

[57] Couckuyt, I., Deschrijver, D., and Dhaene, T. (2014). Fast Calculation of Multiobjective Probability of Improvement and Expected Improvement Criteria for Pareto Optimization. *Journal of Global Optimization*, 60(3), 575–594. doi:10.1007/s10898-013-0118-2.

[58] Emmerich, M. (2005). *Single-and multi-objective evolutionary design optimization assisted by gaussian random field metamodels*. Ph.D. thesis, Universitt Dortmund, Dortmund, Germany.

[59] Hupkens, I., Deutz, A., Yang, K., et al. (2015). Faster Exact Algorithms for Computing Expected Hypervolume Improvement. In *International Conference on Evolutionary Multi-Criterion Optimization*. Springer, pp. 65–79. doi:10.1007/978-3-319-15892-15.

[60] Deb, K., Pratap, A., Agarwal, S., et al. (2002). A Fast and Elitist Multiobjective Genetic Algorithm: NSGA-II. *IEEE Transactions on Evolutionary Computation*, 6(2), 182–197. doi:10.1109/4235.996017.

[61] Zitzler, E., Laumanns, M., and Thiele, L. (2001). SPEA2: Improving the Strength Pareto Evolutionary Algorithm. Tech. Rep. TIK-Report 103, Eidgenössische Technische Hochschule Zürich (ETH), Institut für Technische Informatik und Kommunikationsnetze (TIK).

[62] Pedregosa, F., Varoquaux, G., Gramfort, A., et al. (2011). Scikit-Learn: Machine learning in Python. *Journal of Machine Learning Research*, 12, 2825–2830.

[63] Jones, D. R. (2001). The DIRECT Global Optimization Algorithm. In *Encyclopedia of Optimization*. Springer, pp. 431–440.

[64] Jones, E., Oliphant, T., Peterson, P., et al. (2001–). SciPy: Open source scientific tools for Python. `http://www.scipy.org/`.

[65] U.S. Department of Defence (1998). *Military Handbook, MIL–HDBK–5J: Metallic Materials and Elements for Aerospace Vehicle Structures*, Chap. 6. U.S. Department of Defence, pp. 51–76.

[66] U.S. Department of Defence (1998). *Military Handbook, MIL–HDBK–5J: Metallic Materials and Elements for Aerospace Vehicle Structures*, Chap. 5. U.S. Department of Defence, pp. 43–50.

[67] Dowell, E. H. (1974). *Aeroelasticity of Plates and Shells*, Vol. 1. Springer Science & Business Media. doi:10.1115/1.3423871.

[68] Gibson, L. J. and Ashby, M. F. (1999). *The Mechanics of Honeycombs*, Chap. 4. Cambridge University Press, pp. 69–119. doi:10.1017/cbo9781139878326.006.

[69] Swann, R. T. and Pittman, C. M. (1961). Analysis of Effective Thermal Conductivities of Honeycomb-Core and Corrugated-Core Sandwich Panels. Tech. Rep. TN D-714, NASA.

## ACKNOWLEDGEMENT

This research was funded by the FXB Center for Rotary and Fixed Wing Air Vehicle Design (FXB-CRFWAD). In addition, the first author gratefully acknowledges the support of the Rackham Predoctoral Fellowship awarded by the Univeristy of Michigan.

## COPYRIGHT STATEMENT